RSC Advances

ROYAL SOCIETY OF CHEMISTRY

PAPER

View Article Online
View Journal | View Issue

Cite this: *RSC Adv.*, 2026, **16**, 2093

Bio-adsorbent for wastewater treatment: amination of green coconut husk waste-derived lignin for the removal of Congo red dye

Riyadh Hossen Bhuiyan, [a] Mohammad Mahbubur Rahman, *[a] Md. Masum Billah, [b] Md. Fardin Ehsan,[a] Taslima Akter,[c] Md. Shakhawoat Hossain, [d] Md. Mamunur Rashid,[e] Md. Saiful Islam [f] and Swapan Kumer Ray *[a]

Aminated lignin (AmL) has significant potential as a superior bio-adsorbent due to its unique structure and properties. In this study, AmL was synthesized by a Mannich reaction from coconut fiber alkali lignin (CFAL). The structure of CFAL and AmL was confirmed with the help of FT-MIR, ^{1}H-NMR spectroscopy, and CHNS elemental analysis. The crystallinity, morphology, and thermal properties were measured using XRD, SEM, and TGA, respectively. Finally, AmL was used to remove the anionic Congo red (CR) dye from an aqueous solution to investigate the performance of AmL compared to CFAL. The effect of pH, dose of adsorbent, and concentration of dye solution was investigated. 95.5% of the CR dye was removed within 80 minutes at pH 5 from a 20 ppm solution using 0.025 g of AmL. The dye removal efficiency of AmL samples was better than that of CFAL. This work demonstrates that AmL shows greater promise as a bio-adsorbent and can be further utilized as a green alternative in wastewater treatment. Thermodynamic analysis revealed that the adsorption process is spontaneous and exothermic, with negative Gibbs free energy ($\Delta G°$) and enthalpy ($\Delta H°$) values; AmL ($\Delta H° = -52.06$ kJ mol^{-1}) displayed a stronger adsorption affinity than CFAL. In addition, reusability studies demonstrated that AmL retained 83.4% of its adsorption efficiency after four adsorption–desorption cycles, highlighting strong operational stability compared with CFAL. To complement the experimental findings, density functional theory (DFT) and time-dependent DFT (TD-DFT) calculations were carried out at the B3LYP/6-31G(d) basis set level. The results revealed that amination slightly reduces the HOMO–LUMO band gap (4.761 → 4.747 eV), enhances charge delocalization, and stabilizes excited states through partial n → π* transitions introduced by nitrogen functionalities. Electrostatic potential (ESP) mapping further demonstrated moderated charge localization and more uniform surface polarity in AmL, providing additional active sites for electrostatic interactions and hydrogen bonding with CR dyes. The theoretical insights are consistent with the experimental findings, indicating that electronic modification *via* amination enhances both adsorption affinity and charge-transfer efficiency.

Received 5th October 2025
Accepted 28th December 2025

DOI: 10.1039/d5ra07573d

rsc.li/rsc-advances

1. Introduction

Freshwater, a finite natural resource crucial for the survival of ecosystems, faces challenges due to the global population surge and rapid industrial development. Presently, over 8 billion people contend with severe freshwater shortages.[1] The necessity of clean water is increasing rapidly due to rapid urbanization and industrialization. The textile industry is one of the sectors that utilizes substantial amounts of natural water for its various processes. The wastewater released from the textile industry typically contains toxic pollutants, particularly organic dyes, as well as heavy metals that can pose serious environmental concerns.[2,3] Dyes are used as colorants not only in the textile industry but also in the plastic, paper, leather, and food industries.[4] About 7 00 000 tons of dyes, most of which are

[a]*Principal Scientific Officer, Fibre & Polymer Research Division, BCSIR Dhaka Laboratories, Bangladesh Council of Scientific and Industrial Research (BCSIR), Dhanmondi, Dhaka-1205, Bangladesh. E-mail: mahbub.bcsir@yahoo.com; swapanray_bcsir@ymail.com; Tel: +8801911776171; +8801534149306*

[b]*Department of Applied Chemistry and Chemical Engineering, Gopalganj Science and Technology University, Gopalganj, Dhaka, Bangladesh*

[c]*Department of Theoretical and Computational Chemistry, University of Dhaka (DU), Dhaka-1000, Bangladesh*

[d]*Ahsanullah University of Science and Technology (AUST), Dhaka-1208, Bangladesh*

[e]*Institute of Food Science and Technology (IFST), Bangladesh Council of Scientific and Industrial Research (BCSIR), Dhanmondi, Dhaka-1205, Bangladesh*

[f]*Pharmaceutical Sciences Research Division, BCSIR Dhaka Laboratories, Bangladesh Council of Scientific and Industrial Research (BCSIR), Dhanmondi, Dhaka-1205, Bangladesh*

organic, are produced annually, and about 10–15% of these dyes are released as effluents from these industries.[5,6] Organic dyes exhibit poor biodegradability and toxicity, causing serious harm not only to aquatic life but also to humans.[7,8] As a result, an efficient dye removal method is imperative to minimize these issues.

Several wastewater treatment methods have been used, and numerous studies have focused on effectively removing organic dyes from wastewater. The techniques utilized to remove these dyes by coagulation/flocculation,[9,10] adsorption,[11] ion exchange,[12] membrane separation,[13] chemical oxidation,[14] and biological treatments.[15] Among these, the adsorption method is efficient due to its low cost, ease of handling, and energy-saving features.[16] The adsorption of dyes is facilitated by hydrogen bonding and electrostatic interactions.[17] Organic dyes can be categorized based on their charge in aqueous solutions as cationic (basic dyes), anionic (acid, direct, reactive dyes), or nonionic (disperse dyes), and among these azo dyes are widely used in the textile industry for their affordability and superior coloring properties.[18,19] The majority of azo dyes are categorized as anionic dyes, making them the preferred choice for industrial applications.[20,25] A range of inorganic and organic materials, including activated carbon, lignocellulosic materials, zeolite, graphite, and graphene oxides, have been utilized for removing organic dyes in wastewater treatment.[21,22] These materials exhibit varying adsorption activities, with some displaying exceptional performance in removing dyes. The selection of the adsorbent should consider its functionality, adsorption capability, and environmental friendliness.

Lignin is one of the significant constituents of plants and trees, and it is the most abundant after cellulose. It is a phenylpropane-based natural aromatic polymer featuring various functional groups, including carbonyl, methoxy, carboxyl, and hydroxyl groups.[23] Due to the presence of different functional groups, lignin can be chemically modified to introduce functionalities. Most of the lignin is separated from pulp and paper-making processes, and on average, 50 million tons of lignin are produced annually. However, most of the lignin is utilized as low-grade boiler fuel and for thermal recycling.[24,25] Only about 2% of the lignin is used for chemical and material applications.[26] Thus, lignin needs to be converted into valuable products, as it has the potential to be not only practical but also eco-friendly. The amination of lignin offers a viable approach to enhance the adsorption capability of lignin through functionalization. Lignin amination involves the introduction of an amine group into the lignin backbone, thereby increasing the number of adsorption sites. The amino group, which contains an electronegative nitrogen atom, readily protonates and forms hydrogen bonds. Under acidic conditions, the amino group undergoes conversion into positively charged ammonium ions, facilitating the effective adsorption of anionic dyes.

Recent studies have focused on the excellent adsorption capability of lignin and have extensively utilized it as an adsorbent to remove harmful organic dyes from wastewater.[27] Earlier studies on adsorption involving lignin have focused on removing heavy metals from wastewater.[28,29] Recent research has explored removing organic pollutants, including persistent organic pollutants (POPs) such as dyes and pesticides, from wastewater by utilizing lignin as both single and hybrid composites. One advantage of lignin is its affinity for both cationic and anionic dyes, which encompass the majority of industrially applied dyes. Polyaniline (PANI)-lignin composites are one of the adsorbents that exhibit a significant removal of the anionic azo dye Congo Red.[27] This composite is also utilized as an adsorbent in another study for the removal of Reactive Black 5, a similarly anionic azo dye.[30] In other studies, lignin-based hydrogels are also utilized as excellent adsorbents for dye removal, as lignin contains various functional groups capable of forming electrostatic interactions with pollutants.[31,32] Hybrid composites such as lignin–chitosan have been utilized as effective adsorbents for dye removal.[33,34] Parajuli *et al.* utilized a two-step approach to synthesize an aminated cross-linked lignophenol for metal ion adsorption.[35] Wang *et al.* synthesized aminated lignin using the Mannich process and evaluated its efficacy in decolorizing anionic azo dyes.[36] Heo *et al.* synthesized amino-silane-modified lignin to remove cationic and anionic dyes from aqueous solution.[37]

This study introduces the use of CFAL, underutilized agricultural byproduct, as a source for making improved adsorbents. The creation of AmL through the Mannich reaction offers a more eco-friendly alternative to other intricate lignin modification methods. By integrating experimental adsorption tests with DFT/TD-DFT calculations and ESP mapping, this study delivers molecular-level insights into how amination boosts adsorption by reducing the HOMO–LUMO gap, enhancing charge delocalization, and increasing active sites. This research highlights AmL as a sustainable and high-performance bio-adsorbent, with promising applications in environmentally friendly dye wastewater treatment.

2. Materials and methods

2.1. Materials

Green coconut husk waste materials were used as the source of alkali lignin. The green coconut husk waste materials were collected from Dhaka city, Bangladesh. Sodium hydroxide, sulfuric acid, anthraquinone, glacial acetic acid, diethylamine, 1,4-dioxane, and formaldehyde (37%), dimethyl sulfoxide (DMSO), and hydrochloric acid (37%) were procured from Sigma Aldrich, while DI-water was obtained from AFC chemicals ltd.

2.2. Preparation of AmL

2.2.1. Isolation of lignin from green coconut husk wastes and purification. The isolation of lignin from green coconut waste fibre was carried out following a soda-anthraquinone pulping process with some modifications.[38] The materials were washed with water and dried at room temperature. It was cut into small pieces. A total of 100 g of green coconut fibre (GCF) was placed in an RB flask containing 500 mL of 0.7% H_2SO_4 and left to soak overnight to remove hemicellulose. The samples were then filtered and dried at room temperature. Subsequently, 1 L of 7% (w/v) NaOH and 0.2% (w/v)

Table 1 Mannich reaction of CFAL in aqueous dioxane with diethylamine [$NH(C_2H_5)_2$], formaldehyde (HCHO), and acetic acid (AcOH) at 65 °C

	Reaction conditions				
Sample	$NH(C_2H_5)_2$ (mmoL)	HCHO (mmoL)	Time (h)	AcOH (mL)	Yield (%)
R1	5	5.0	4	1.0	225
R2	5	6.0	4	1.0	230
R3	5	7.0	4	1.0	273
R4	5	7.5	4	1.0	235
R5	5	8.0	4	1.0	240

anthraquinone were added to the treated GCF in a sealed steel chamber, and the temperature was maintained at 170 °C for 1 h. After pulping, the heated black liquor was allowed to cool for 12 h at room temperature in an open vessel before being filtered using a silk cloth. The separated pulp was stored, and the black liquid was subjected to further treatment. Lignin was purified from the black liquor according to Abdul Latif *et al.*[39] with a few modifications. To precipitate the lignin, 10% H_2SO_4 was added to a portion of the liquid in a 1 L beaker. Additional H_2SO_4 was added to lower the pH of the solution to 2.5 at 30 °C. The mixture containing the precipitate was then centrifuged for 10 min at 8000 rpm in centrifuge tubes. The precipitated material was dried for 24 hours at 60 °C in a vacuum oven, yielding 35.5 g of dried mass. The obtained lignin was termed CFAL. The obtained lignin may contain ash. The obtained lignin was further purified using the method described by Gilarranz *et al.*[40] A total of 35.5 g of CFAL was added to 100 mL of 3% (w/v) H_2SO_4 in a flask and heated for 2 h at the boiling point. After the refluxing process was complete, the mixture was filtered and washed multiple times with distilled water. Subsequently, the mass was dried at 60 °C in a vacuum oven for 24 h.

2.2.2. Amination of the CFAL. The amination of CFAL samples was performed using a Mannich reaction protocol described in.[41] The reaction conditions are presented in Table 1. The amination reaction of lignin and its mechanism are illustrated in Fig. 1. A certain amount of CFAL (*ca.* 0.2 g) was dissolved in dioxane aqueous solution, followed by the addition of aqueous solution of diethylamine, formaldehyde, and glacial acetic acid. This mixture was then heated at 65 °C for 4 hours under rigorous stirring. After reaction, the final product was dried in a vacuum dryer to remove most of the organic reagents. Subsequently, the product was purified using a dialysis tube with a molecular weight cutoff of 1000 Da, followed by freeze-drying.[42]

2.3. Proximate analysis

2.3.1. Determination of moisture content. GCF, even after being vacuum-dried, still contained trapped water inside the granules. The total moisture content of GCF was determined by using a classic laboratory method. In this technique, 20.0 g of the sample was taken in a Petri dish, and the total weight of both was taken using a digital weight balance. Then the sample was heated to 105 °C for 4 hours in an oven and cooled in the dry atmosphere of a desiccator. Then the final weight was taken. The moisture content of the sample is simply the percentage of weight lost after the sample has been thoroughly dried.

$$\text{Moisture content, } \mathrm{MC}(\%) = \frac{W}{W_1} \times 100\% \quad (1)$$

W = weight of water, W_1 = weight of GCF.

2.3.2. Determination of ash content. Determine the sample's oven-dry mass (ODM) using an air-dry sample. Calculate and note the ash % using the ODM basis. Ash content is determined by NREL/TP-510-42622, LAP for total solids in biomass.

$$\%\mathrm{Ash} = \frac{\mathrm{mass}_{\text{crucible with ash}} - \mathrm{mass}_{\text{crucible}}}{\mathrm{ODM}_{\text{sample}}} \times 100 \quad (2)$$

2.4. Elemental analysis of CFAL and AmL samples

The C, N, and H were analyzed using a CHNOS (Elementar Analysen systeme GmbH, Germany). Standard KNO_3 solutions with concentrations ranging from 1 to 100 ppm were used to calibrate the system.

2.5. Measurement of intrinsic viscosity

The intrinsic viscosity of CFAL and AmL were measured using 0.5 N NaOH solutions at 303.2 K. The Anton Paar

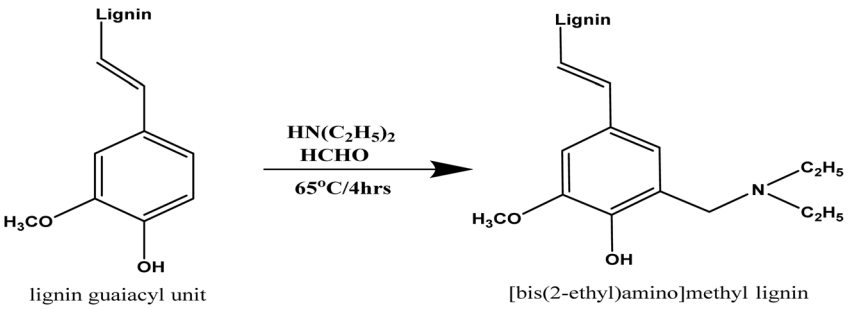

Fig. 1 Schematic amination reaction of lignin.

microviscometer (Lovis 2000 M, 81686360 using the capillary tube LOVIS FLOW-THROUGH FILLING SET 1.59, Serial No. 19391250) was used to measure viscosity. The rolling ball (batch 1412/125334/Au 01/4, density 7.90 g cm^{-3} and diameter 1.5 mm gold 4) was used. The samples were filtered through a 45 μm disk filter. The density of the solvent was measured using an automated density meter (Model DMA 5000M; Anton-Paar, Austria). The intrinsic viscosities of isolated CFAL and AmL were calculated using the Billmeyer equation (eqn (3))

$$[\eta] = \frac{0.25 \times [\eta_r - 1 + 3\ln \eta_r]}{c} \quad (3)$$

where, $[\eta]$ is the intrinsic viscosity, η_r is the relative viscosity, and c is the amount of polymer in g mL^{-1} of the solution.

2.6. FT-IR spectroscopic analysis

The moisture-free lignin samples were analyzed using an FT-IR Spectrometer (Frontier, PerkinElmer, UK) equipped with an attenuated total reflectance accessory. The spectra were recorded in the range of 400–4000 cm^{-1} with a spectral resolution of 4 cm^{-1} and 32 scans.

2.7. ^{1}H, ^{13}C and HSQC NMR spectroscopic analysis

^{1}H, ^{13}C and HSQC NMR spectra of the lignin samples were recorded utilizing an inverse gated proton decoupling sequence and a 5-mm BBO probe on a Bruker Avance III 600 MHz spectrometer (Bruker, Germany). Spectra of the lignin samples were obtained to evaluate the lignin structure before and after treatment. DMSO-d_6 was utilized as a solvent for the investigation of unmodified and modified lignin.

2.8. Thermogravimetric analysis

TGA analysis of the lignin samples were performed using a TGA 601 series instrument (Leco model) under a N_2 atmosphere, with a temperature range of 30 to 800 °C and a heating rate of 10 °C min^{-1}, employing an Al_2O_3 pan as a reference.

2.9. X-ray diffraction

X-ray diffraction (XRD) analysis was conducted on the selected samples, using an X-ray diffractometer (PerkinElmer, UK). Measurements were taken using Cu Kα radiation ($\lambda = 1.541$ Å), with diffraction patterns recorded over a 2θ range of 5° to 80°. Data acquisition was performed at a scan rate of 0.05° s^{-1} with a step size of 0.02°. The instrument operated at an accelerating voltage of 40 kV and a current of 30 mA. The resulting diffraction profiles were analyzed to determine the crystallographic properties and interlayer spacing of the samples.

2.10. Scanning electron microscopy

Scanning electron microscopy (SEM) was employed to examine the surface morphology of selected materials using an EV018 SEM instrument (Carl Zeiss AG, Germany). To ensure optimal imaging quality and prevent charging, the samples were mounted on carbon adhesive tape and then sputter-coated with a thin layer of platinum to enhance electrical conductivity. Imaging was conducted under high vacuum conditions at varying magnifications to capture detailed surface features. The acquired micrographs were subsequently analyzed to evaluate the surface texture and microstructural characteristics of the samples.

2.11. Adsorption study of CFAL and AmL samples

In this study, the effect of various parameters, including pH, dye concentration, and adsorbent dosage, was evaluated on the adsorption performance of lignin samples. A beaker was filled with 50 mL of an aqueous CR with a specific concentration. The pH of the solution was varied from 3 to 10 using 0.1 M HCl and 0.1 M NaOH. Next, a predetermined weight of adsorbent was added to the solution, and the mixture was stirred for 0 to 120 minutes. Filtrate samples are measured the final concentration by UV-VIS spectroscopy (PerkinElmer Lambda 35). The adsorption capacity and dye removal percentages were calculated using eqn (4) and (5)

$$Q_e = \frac{C_i - C_e}{M} \times V \quad (4)$$

$$R(\%) = \frac{C_i - C_e}{C_i} \times 100 \quad (5)$$

where C_i is the initial concentration of dye in a control sample (mg L^{-1}), C_e is the residue concentration of dye after the adsorption experiment by lignin and aminated lignin samples (mg L^{-1}), and M (g) is the mass of the adsorbent.

2.12. Computational methods

All calculations were carried out using Gaussian 09W[43] and visualized with GaussView 6.0. The ground-state geometries were fully optimized at Becke's 3-parameter hybrid interchange functional B3LYP/6-31G(d)[44] level of theory, incorporating the implicit model- Conductor-like Polarizable Continuum Model (CPCM)[45] solvation model to account for water as the solvent. Frontier molecular orbitals (HOMO and LUMO) were analyzed to evaluate the electronic distribution and energy gaps. Time-dependent DFT (TD-DFT)[46] calculations were subsequently carried out at the same level of theory to investigate the low-lying singlet excited states, corresponding absorption wavelengths, and oscillator strengths. This approach enabled detailed insight into the electronic structure of the molecules in an aqueous environment.

3. Results and discussion

3.1. Characterization of isolated CFAL and synthesized AmL

3.1.1. Proximate analysis of green coconut husk waste. The compositional analysis of the green coconut husk waste was determined using standard analytical techniques, as described in the National Renewable Energy Laboratory report NREL/TP-510-42618.[47] The Cross & Bevan method[48] was used to evaluate the substance in green coconut husk. The moisture content of the green coconut husk was 8.2%. The data for the compositional analysis of green coconut husk showed that 38.75%

Klason lignin was obtained. A similar experiment was conducted by Abd Latif *et al.*[39] They also found 21.74% of Klason lignin in green coconut husk.

3.1.2. Isolation and purification of CFAL. According to the empirical formula, the structure of lignin was $C_9H_{7.96}O_{2.83}(-OCH_3)_{0.915}$. Lignin was isolated from the black liquor obtained through the soda-anthraquinone (NaOH-AQ) pulping process of green coconut husk waste. 28.2% of lignin was found in the black liquor. As the conditions of the alkaline pulping process were more severe, the delignification process of lignin from coconut husk was quicker and more effective.[49] Significant research has been conducted to isolate lignin from coconut husk. Gilarranz *et al.*[50] employed a different pulping method for extracting lignin from coconut husk. They found that 33 wt% of lignin was obtained from NaOH-AQ. They also investigated the NaOH-AQ system as the most appropriate isolation process for coconut husk lignin, due to the low degree of chemical modification of the lignin obtained with this approach. It has the potential to be used in situations when further chemical interactions with lignin are required. CFAL extracted with NaOH at high temperatures and in the presence of anthraquinone yields more soluble acetylated fractions. Panamgama *et al.*[51] conducted various pulping protocols for removing lignin from coconut coir pith, a biomass source. They found that the alkaline pulping method yielded the maximum lignin content of 26 wt%. Anuchi *et al.*[52] used ionic liquids as green solvents for the extraction of lignin from coconut husk waste and found 41 wt% of lignin. In this research, the obtained lignin contained 0.61% ash, which was removed by the 3% (w/v) H_2SO_4 treatment. The suspended solids and silica were removed by centrifugation and selective purification, respectively, at pH 5. Then the pH was reduced to 3.5 for the precipitation of lignin.

3.1.3. Amination of CFAL by the Mannich reaction. A Mannich reaction protocol was used to synthesize AmL. The different amination reactions were carried out with variations in the amount of $[NH(C_2H_5)_2]$, HCHO, and AcOH over 4 h at 65 °C. The yields of each reaction are presented in Table 1. The maximum yield (273%) of AmL was obtained with the reaction of 2 mmol of $[NH(C_2H_5)_2]$, 2.2 mmol of HCHO, and 0.4 mL of AcOH in 4 h at 65 °C. The reaction involves the addition of dialkylaminomethyl groups *via* the iminium ion formed by the reaction between formaldehyde and the amine group. It was conducted under acidic conditions to facilitate the formation of the iminium ion as an intermediate species. In alkaline conditions, the *N*,*N*-dialkylaminomethanol group is formed instead of the iminium ion, which is a weaker electrophile than the latter. The lignin structure contains various groups, including guaiacyl, syringyl, and hydroxyphenolic groups.[54,55] Only the guaiacyl and hydroxyphenolic groups are capable of undergoing amination reaction due to the availability of their electron-rich *ortho* sites. The *ortho* position of phenolic guaiacyl units of lignin are available for the amination reaction.[53] Du *et al.*[54] conducted the Mannich protocol for the amination of lignin. They found that within the lignin structure, the C-5 position of the phenolic guaiacyl unit exhibits a high electron density, making it susceptible to nucleophilic attack. Thus, certain amino-alkyl groups can be introduced at this position, specifically at the *ortho* positions of the phenolic hydroxyl in hydroxyphenyl nuclei. Jiao *et al.*[42] characterized lignin using ^{31}P, ^{13}C, and 2D-HSQC NMR spectroscopy and found that guaiacyl phenolic hydroxyl groups (0.00117 mol g^{-1}) and *p*-hydroxyphenyl phenolic hydroxyl groups (0.00087 mol g^{-1}) in the lignin, which contain one and two active sites for Mannich reaction, respectively.

3.1.4. Elemental analysis of CFAL and AmL. Lignin, a natural aromatic polymer made up of 4-hydroxyphenylpropanoids linked by ether and carbon–carbon bonds, is recognized for its complex structure. The degree of amination reaction of lignin could be determined by the determination of nitrogen content in lignin and aminated lignin. The C, H, N, and O content of the isolated CFAL and synthesized AmL samples was analyzed using a CHN elemental analyzer to distinguish between the aminated and non-aminated lignin. The detailed results are tabulated in Table 2, showing the percentage values of C, H, N, and O, as well as the ratios of C and N, and C and H, for assessing the biodegradability of these AmL in soil. Amination of lignin is confirmed from the presence of elemental N in the prepared AmL samples. There was no N found in the isolated CFAL sample. The N content in the aminated samples R1 to R5 was found to be 5.59–6.83%. The introduction of N content into the CFAL backbone confirms the successful amination of lignin. Pan *et al.*[55] measured the N content in the aminated lignin and found that the aminated lignin contained 5.31–6.95% of N. The maximum N content was found in reaction R3, which was 6.83%. This result indicates that more amino groups have been introduced into the lignin structure. These results are consistent with those obtained in reaction R3 (Table 1), where the maximum yield was 273% of AmL with a reaction time of 4 h at 65 °C using 2 mmol of $[NH(C_2H_5)_2]$, 2.2 mmol of HCHO, and 0.4 mL of AcOH.

The nitrogen content increased from 0 to 6.83%, indicating that diethylamine was successfully grafted onto the lignin during the reaction. The amination of soda lignin was found to increase nitrogen and hydrogen in lignin after the amination process.[41] When the C/N ratio of lignin-based products is less than 20, it has been claimed that soil microorganisms can quickly break it down and liberate the organically bound nitrogen.[56] The outcomes showed that the C/N mass ratios of all the products ranged from 8 to 11, and were substantially lower than 20, suggesting that the prepared samples are highly biodegradable in soil.[42]

Table 2 CHNS content of CFAL, and AmL samples, and C/N, C/H are mass percent

	Element mass (%)					
Sample	N	C	H	O	C/N	C/H
CFAL	0	61.48	5.546	30.97	0	11.09
R1	5.59	59.66	8.014	26.74	10.67	7.44
R2	6.36	53.26	7.873	32.51	8.37	6.77
R3	6.83	60.73	7.112	25.68	9.37	8.54
R4	6.70	55.41	7.060	30.83	8.27	7.85
R5	6.48	55.39	7.660	30.12	8.11	7.23

Table 3 Intrinsic viscosity measurement of CFAL and AmLs solution at $T = 25$ °C

Samples	CFAL	R1	R2	R3	R4	R5
Intrinsic viscosity (mL g^{-1})	5.24	5.5173	5.5413	7.421	8.8688	7.730
Molecular Weight(kDa)	60.433	75.633	77.074	274.431	595.613	255.592

3.1.5. Intrinsic viscosity measurement of CFAL and AmL solution. To determine the molecular weight of CFAL and AmL, the intrinsic viscosity of these compounds was measured and is presented in Table 3. Investigations were conducted in aqueous solutions at 25 °C. The viscosity average molecular weight of a polymer can be determined using the Mark–Houwink equation $[\eta] = KM^{\alpha}$. This equation relies on two parameters, K and α, which are influenced by factors such as the type of solvent, the measurement temperature of viscosity, and the kind of polymer.[57] According to the Mark–Houwink equation, a higher molecular weight (M) of a polymer results in a greater intrinsic viscosity ($[\eta]$) at a given weight concentration. In other words, as the molecular weight increases, so does the inherent viscosity. The intrinsic viscosity of CFAL is lower than that of AmL, suggesting an increase in the molecular weight of AmL after amination.

3.1.6. FT-IR spectroscopic analysis of CFAL and AmL. The FT-IR spectra of CFAL and AmL have been displayed in Fig. 2 and 3. The obtained bands from FT-IR spectra have been assigned with possible vibration in this paragraph. It was evident from the spectra that these compounds exhibited characteristic lignin absorption peaks. For instance, it is believed that the hydroxyl groups in aliphatic and phenolic molecules are responsible for the broad peak at 3361 cm^{-1}.[42] The peaks at 2936 cm^{-1} and 2844 cm^{-1} correspond to the C–H stretching vibrations in the methyl and methylene structures, respectively. The peak at 1701 cm^{-1} was assigned for C=O bonds in unmodified alkali lignin, and bands at 1596 cm^{-1} and 1514 cm^{-1} were the aromatic skeletal stretching vibrations of lignin.[58] In particular, the bands at 1262 cm^{-1} and 1218 cm^{-1} indicate guaiacyl (G) ring and C=O stretching vibrations, respectively. The bands at 1117 cm^{-1} is connected to aromatic in-plane deformation of C–H stretching, and were identified as signals attributed to G units, which indicate that the Mannich reaction did not damage the skeletal structure of lignin.[59] It can be seen that, few absorption bands in AmL are more intense compared to CFAL. For example, the spectrum of AmL showed a fierce absorption peak at 2960 cm−1, indicating the vibration of the C–H bond in CH_2. The C–O and C–N bonds have a relationship with the increased band intensity at 1090 cm^{-1}. Additionally, the C–N bonding peak at 1362 cm^{-1} and the substantial peak intensity at 1458 cm^{-1} are both associated with the vibration of amine groups in the AmL samples.[60] The peak intensities of 1598 cm^{-1}, 1517 cm^{-1}, 1459 cm^{-1}, and 830 cm^{-1} were attributed to aromatic C–H vibrations, which are lessened in AmL due to the amination of the aromatic areas following the Mannich reaction.[36] Moreover, the peak at 1701 cm^{-1}, which is related to the vibration of the C=O bonds, is more intense in the aminated lignin than in CFAL.[59]

The Table 4 provided seems to be derived from FTIR (Fourier Transform Infrared) data analysis, presenting the functional groups per unit CFAL (unit: mmol g^{-1}), which presents a specific characteristic of the sample's molecular structure, often used to analyze the lignin content and its structure, providing insights into its chemical properties and behavior. The S/G ratio is 0.5337, which means that there are more G units than S units because the ratio is less than 1. A ratio above 1 would indicate more Syringyl units (S), and a ratio below 1 shows a higher proportion of Guaiacyl units (G). As a result, the S/G ratio of 0.5337 suggests that the sample has a greater proportion of Guaiacyl (G) units compared to Syringyl (S) units.

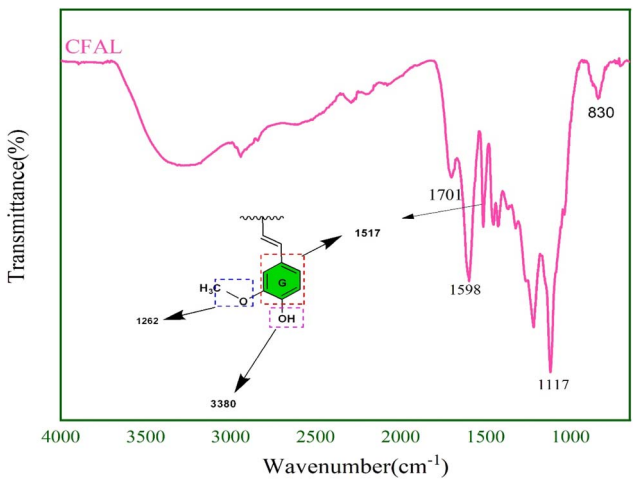

Fig. 2 FT-IR spectra of CFAL.

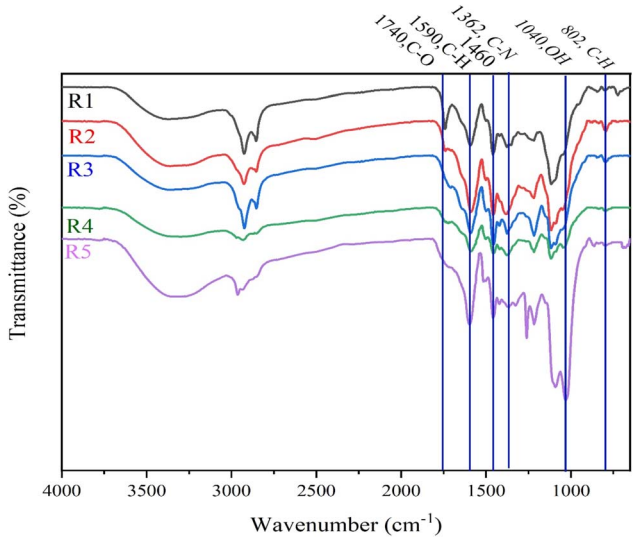

Fig. 3 FT-IR spectra of the AmL (R1–R5) samples.

Table 4 Functional group per unit CFAL (mmol g^{-1})[61]

OH total	Ar–OH groups	O–CH_3 groups	C=O groups	S/G ratio	Remarks
0.9576	0.7667	0.83	0.7861	0.5337	CFAL

3.1.7. NMR spectroscopic analysis of CFAL and AmL samples

3.1.7.1 ^{1}H-NMR spectroscopic analysis. The ^{1}H-NMR spectra of CFAL and AmL are shown in Fig. 4, providing clear evidence of the successful conversion of CFAL into AmL. In both spectra, a signal at 3.7 ppm corresponds to the methoxyl group. The CFAL spectrum (a) exhibits a strong signal in the aromatic region (6.5–7.8 ppm), confirming the presence of aromatic protons. After the Mannich reaction, this signal intensity is markedly reduced, indicating that amine groups have bonded to the aromatic ring in AmL.[60] In the AmL spectrum (b), ethyl protons appear in the region 1.00 and 2.61 ppm,[61] while an additional signal at 3.71 ppm is attributed to amine groups [–N–CH_2–Ar]. The phenolic protons are observed at 8.6 ppm in CFAL[62] and shift to 9.4 ppm in AmL, further confirming structural modification.[51] Taken together, these spectral changes—reduced aromatic proton signals, the emergence of ethyl and amine peaks, and the shift in phenolic proton signals—demonstrate that the Mannich reaction effectively introduces amine functional groups into the lignin structure. Overall, the ^{1}H-NMR spectra provide comprehensive evidence of the successful amination of CFAL.

3.1.7.2 ^{13}C and ^{1}H–^{13}C HSQC NMR spectroscopic analysis. To study the chemical structural changes of CFAL during the

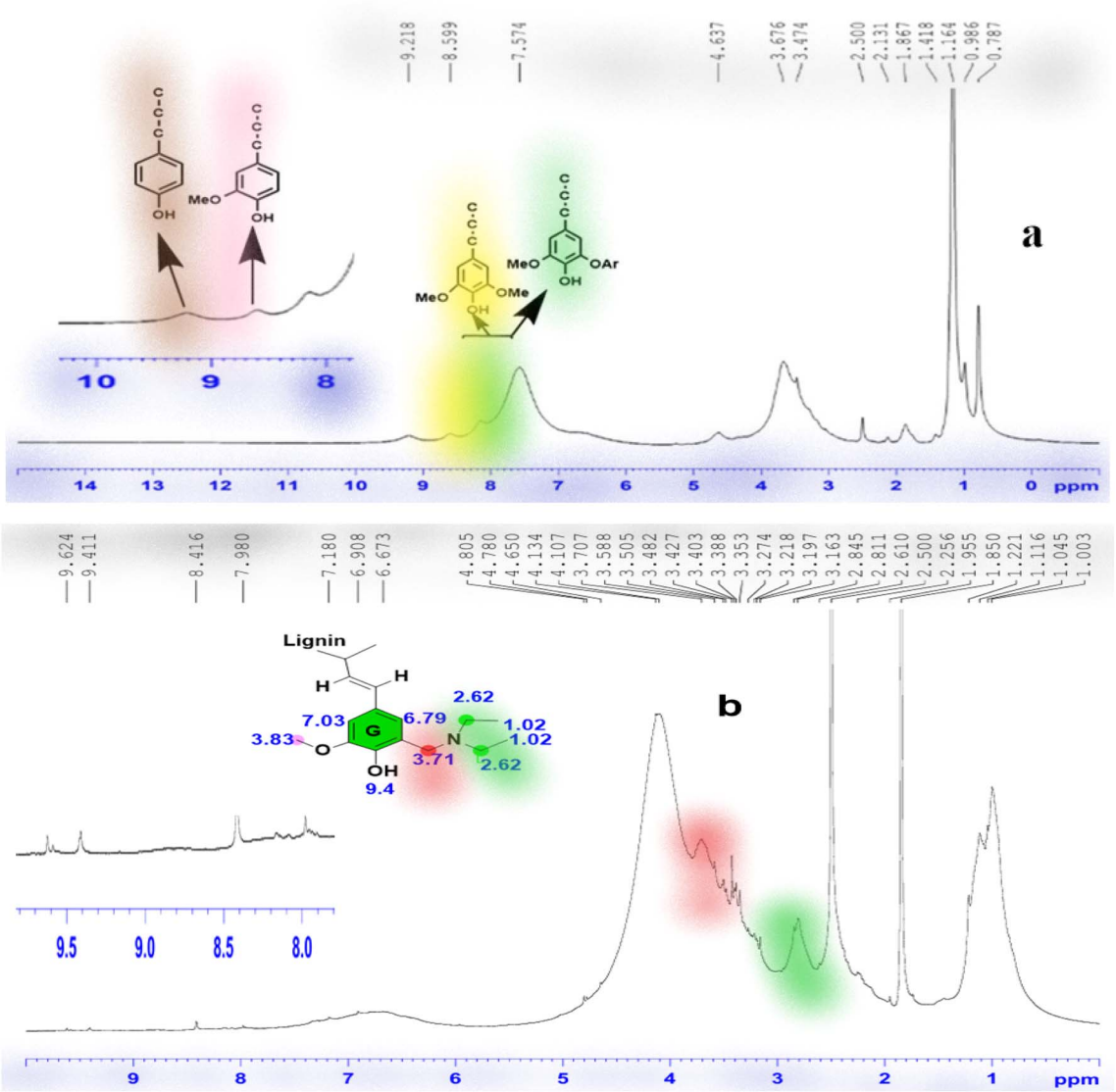

Fig. 4 ^{1}H-NMR spectra of (a) CFAL and (b) AmL of R3

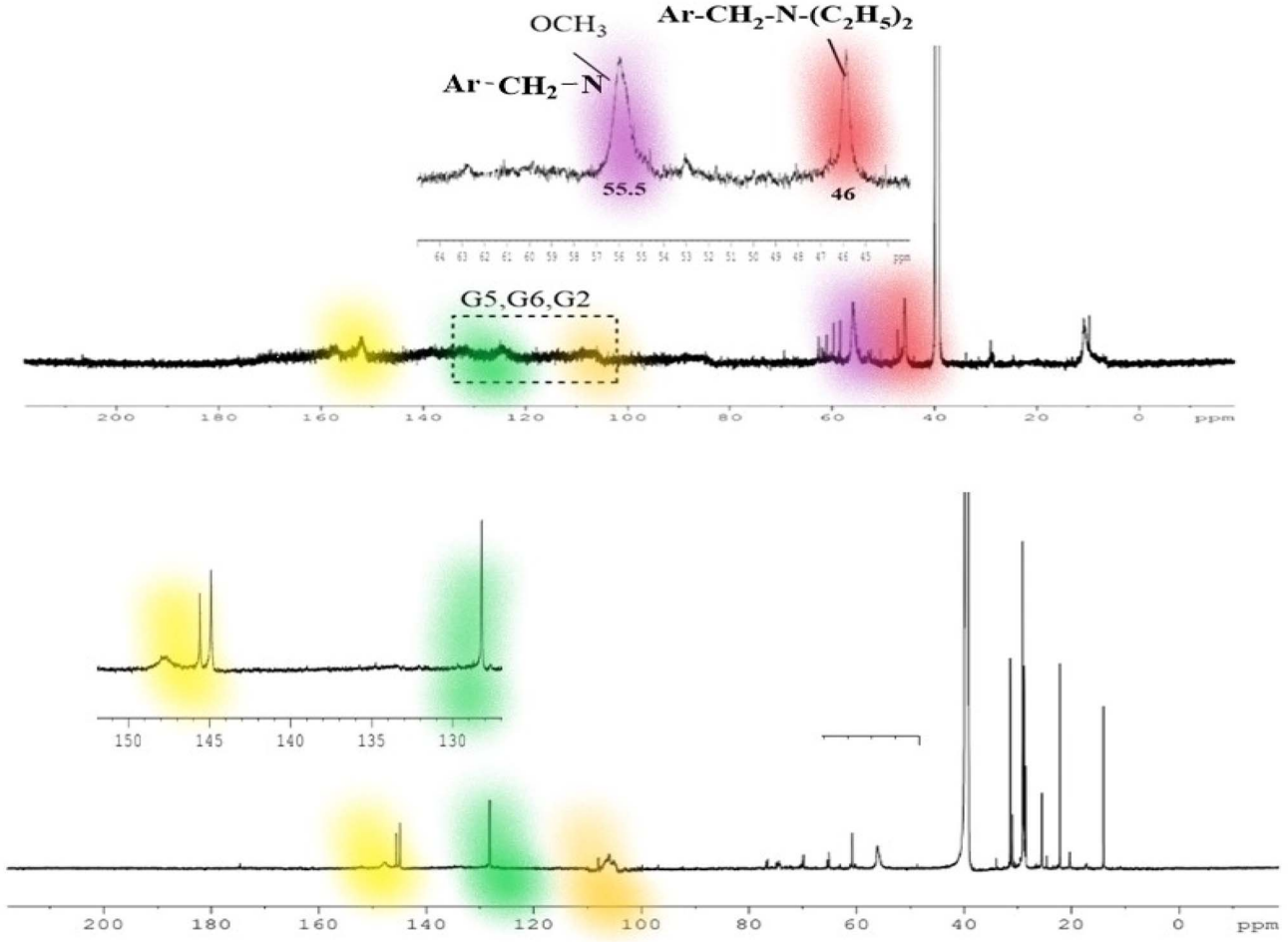

Fig. 5 ^{13}C NMR spectrum of AmL.

Mannich reaction, aminated lignins (AmLs) were analyzed using quantitative 2D-HSQC NMR. The side-chain and aromatic regions in the 2D-HSQC spectra of AmLs (shown in Fig. 5) were similar to those of the original CFAL, indicating that the mild Mannich reaction did not disrupt the CFAL substructure. However, it is important to note that the signal at 60.5/3.50 represents overlapping peaks from methoxy groups and methylene signals from Ar-CH_2N, which could not be distinguished in the lignin amine spectra (Fig. 5).[63] Quantitative analysis of aminated lignin *via* 2D-HSQC revealed structural transformations occurring during the Mannich reaction. Specifically, the proportion of G units in AmLs decreased compared to the corresponding CFALs, due to the Mannich reaction targeting the G5 active sites. The decrease in G units upon amination indicates that the active sites on guaiacyl moieties (particularly the G5 ortho position adjacent to the phenolic hydroxyl) are key reactive centers for electrophilic attack by diethylamine, confirming that lignin's chemical reactivity mainly depends on these electron-dense sites. The Mannich reaction's electrophilic mechanism, involving formaldehyde activation with diethylamine under acidic conditions, facilitates effective grafting of amine functionalities onto lignin.[64] This chemical modification can enhance lignin's reactivity, solubility, and functional properties, making it useful for applications like adsorption, catalysis, and composite fabrication. The mechanism of this Mannich reaction between lignin and diethylamine under acidic conditions is illustrated in Fig. 6.

Quantitative ^{13}C NMR was employed to monitor changes in signal intensities of lignin during the Mannich reaction, and these results were interpreted together with the 2D-HSQC spectra shown for CFAL and AmL. In the aromatic region, most signals had already been assigned in earlier analyses, but particular attention was given to the guaiacyl $G_{5/6}$ signals at 115–125 ppm, which clearly decreased in intensity in AmL relative to the G_2 region (Fig. 10), consistent with substitution at

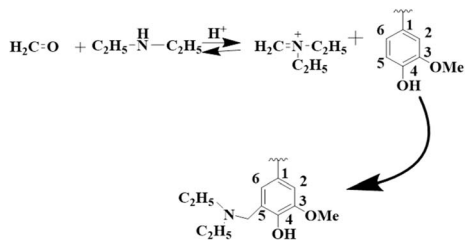

Fig. 6 The mechanism of lignin with diethylamine by the Mannich reaction in acidic medium.

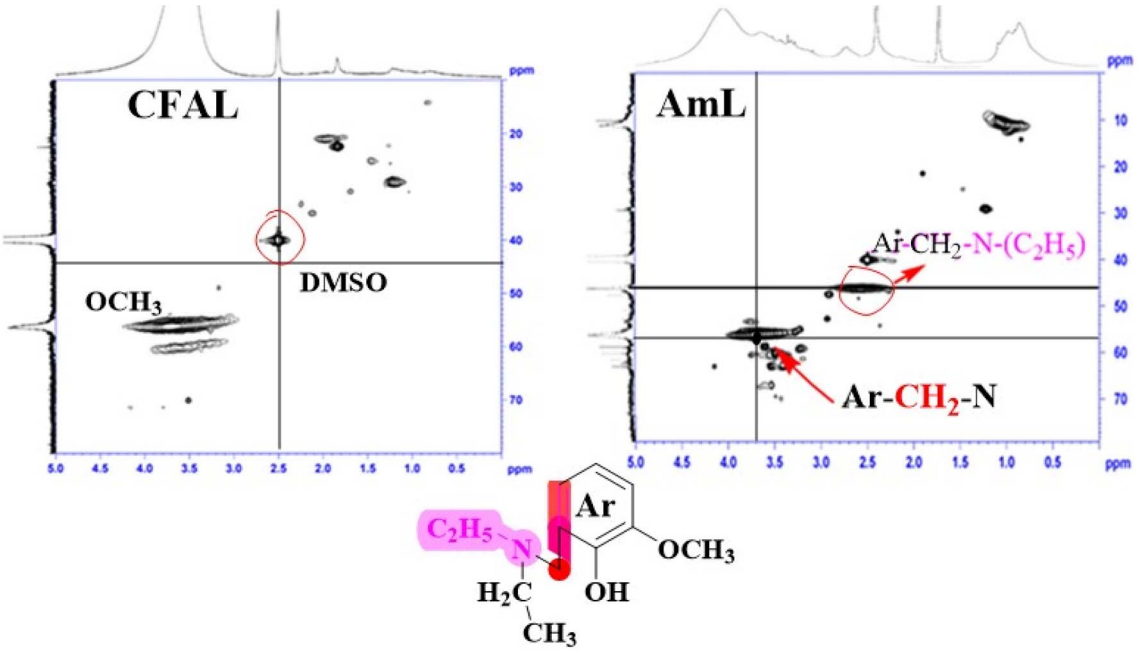

Fig. 7 Aromatic region for CFAL before and after the Mannich reaction under acidic condition.

the G_5 position. Correspondingly, new cross peaks attributable to $N(C_2H_5)_2$ and Ar–CH_2–N, appearing at 46/2.62 and 55.5/3.71 ppm in the AmL spectrum, confirm that diethylamine-containing side chains (Ar–CH_2–$N(C_2H_5)_2$) were introduced onto CFAL during the Mannich reaction, as illustrated by the proposed mechanistic scheme (reaction between formaldehyde, diethylamine, and the guaiacyl unit).

To evaluate possible side reactions, ^{13}C NMR integrals for the aromatic carbons (100–160 ppm) and methoxy carbons (57–54 ppm) were compared between CFAL and AmL (Fig. 7). Using the OCH_3 region (57–54 ppm) normalized to 1, the integrated aromatic-region signals (160–100 ppm) showed only minor differences between CFAL and AmL, indicating that condensation by formaldehyde at C-5 to form stilbene-type structures is minimal and can be largely disregarded.[65] Additional subdivision of the aromatic window into protonated aromatic (125.0–100.0 ppm), condensed aromatic (140.0–125.0 ppm), and oxygenated aromatic (155.0–140.0 ppm) regions provides more detailed insight into how CFAL's aromatic framework is modified during the Mannich reaction: the loss of $G_5/_6$ signal intensity, combined with the emergence of Ar–CH_2–N and Ar–CH_2–$N(C_2H_5)_2$ signals in the 2D spectra, demonstrates that the reaction proceeds selectively at electron-rich G_5 sites while largely preserving the overall aromatic skeleton.[66]

The C–C content in AmLs increased in the 125–140/Ar region, while the C–H content in the 100–125/Ar region decreased, which can be attributed to the replacement of aromatic protons by methylene groups derived from formaldehyde. At the same time, the integrated signal area between 62 and 58 ppm rose to 2.08/Ar because the Ar–CH_2 resonance overlaps with that of β-O-4 linkages, further supporting that the lignin structure has been successfully modified. In Fig. 8, the appearance of new cross peaks corresponding to Ar–CH_2–N and Ar–CH_2–$N(C_2H_5)_2$ in the AmL spectrum, along with the reduced

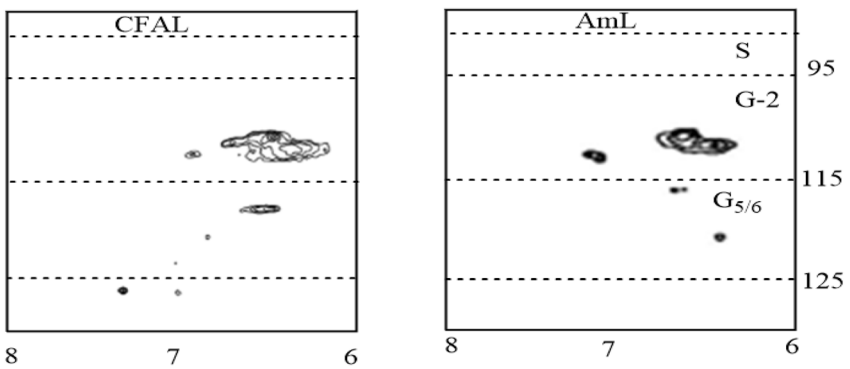

Fig. 8 2D HSQC spectra of the aromatic region for CFAL before and after the Mannich reaction under acidic conditions using diethylamine.

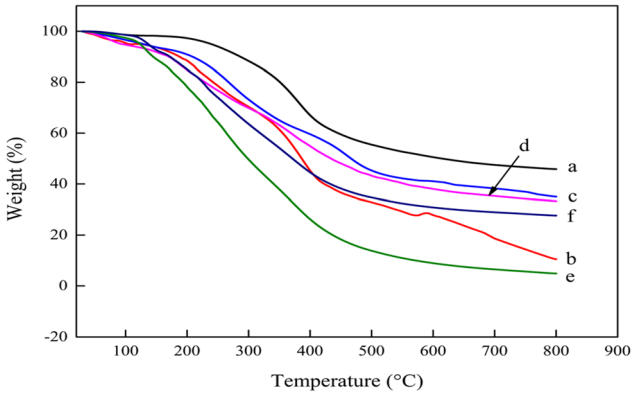

Fig. 9 TGA spectra of (a) CFAL, (b) R1, (c) R2, (d) R3, (e) R4, and (f) R5.

intensity of the $G_{5/6}$ signals, provides clear NMR evidence that diethylamine moieties have been effectively grafted onto CFAL through the Mannich reaction.

3.1.8. Thermal properties of CFAL and AmL samples. The thermogravimetric analysis of CFAL and AmL samples has been presented in Fig. 9, and the degradation behavior of CFAL and AmL samples has been tabulated in Table 5. From Fig. 9, it can be seen that the thermal decomposition rate of all AmL samples is lower than that of CFAL. These results are supported by Jiao *et al.*[42] 2.8 to 22.2 wt% was lost in CFAL and AmL samples up to 200 °C, due to the evaporation of moisture. After that, up to 400 °C, lower molecular weight lignin fragments were evaporated from the CFAL and AmL samples.[36,67] Lignin degradation occurs in two distinct stages. The first stage, which takes place between 150 °C and 260 °C, involves the breaking of α-aryl ether and β-aryl ether bonds. This process leads to dehydration and decarboxylation. The second stage occurs between 260 °C and 480 °C and is characterized by the breaking of C–C bonds between lignin units and the aliphatic side chains of aromatic rings. During thermal degradation, the mass of AmL consistently falls at a constant pace, except for R4. After undergoing thermal degradation, significant amounts of remaining CFAL and AmL samples remain, with residual masses varying from 4.89 to 45.84%. CFAL exhibits superior thermal stability in comparison to AmL. During the modification of CFAL, the syringyl units of lignin do not undergo a reaction, leading to the presence of low-molecular-weight lignin in the aminated derivatives. As a result, aminated derivatives have a larger molecular weight, while the substantial amount of unreacted lower molecular weight components leads to increased weight loss at the same temperatures. As a result, aminated lignin exhibits a more pronounced decrease in weight as the temperature increases during TGA analysis.

3.1.9. X-ray diffraction (XRD) analysis of CFAL and AmL samples. The XRD spectra of CFAL, AmL, and the CR dye adsorbed AmL sample have been presented in Fig. 10. The crystalline nature of all samples is found to be similar. There are no crystalline peaks observed in the spectra. For all samples, peaks at $2\theta = 20°$ indicate the amorphous nature of the samples.[68,69] The sharp peak observed in Fig. 10 corresponds to the sample holder containing aluminum. These identical patterns of CFAL and AmL suggest that the amination of the lignin samples does not introduce a new crystalline phase and the samples are amorphous. Goudarzi *et al.*[68] reported that the diffraction peaks for softwood kraft lignin (SKL) and hardwood kraft lignin (HKL) are at $2\theta = 19.42°$ and $2\theta = 21.25°$, respectively. Crystallite sizes of the carbon present in the lignin samples were determined using the Debye–Scherrer equation, given as follows

$$D = \frac{K\lambda}{\beta \cos \theta} \quad \text{(b)}$$

where D is the average crystallite size, λ is the wavelength of the X-ray in nanometers, β is the full width at half maximum (FWHM) of the XRD peaks, θ is the Bragg angle, and K is a constant value of 0.9.[70,71]

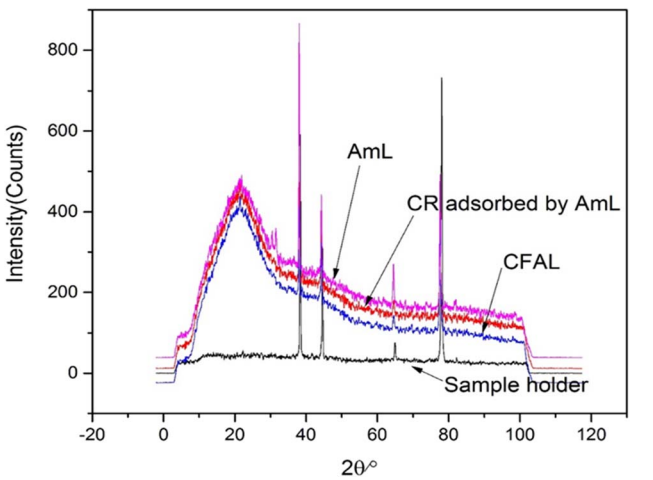

Fig. 10 XRD patterns of isolated CFAL, AmL, and CR adsorber AmL.

Table 5 TGA analysis of CFAL and AmLs

Samples	Weight loss (%) up to 200 °C	Degradation rate at 400–500 °C (%)	50% weight loss up to temperature (°C)	Residual mass at 800 °C (wt%)
CFAL	2.8	32.7–44.7	626	45.84
R1	11.6	54.8–67.2	387	10.49
R2	9.4	40.3–55.0	469	35.04
R3	15.4	45.3–56.9	436	33.31
R4	22.3	74.0–86.4	298	04.89
R5	15.4	55.5–66.4	372	27.64

Table 6 Average crystallite sizes, D of the CFAL, AmL and CR adsorbed AmL

Lignin sample	FWHM, $\beta(\theta)$	Average crystallite size, D (nm)
CFAL	11.19	0.76
AmL	11.52	0.73
CR adsorbed AmL	11.63	0.72

The average crystallite sizes and FWHM for CFAL, AmL, and CR sorbed AmL samples have been presented in Table 6. The values of FWHM and D for all samples are close. Similarly, crystallite sizes of SKL and HKL are 0.67 and 0.75, respectively, and have been reported by Goudarzi *et al.*[68]

3.1.10. SEM analysis of CFAL and AmL samples. Fig. 11 shows SEM images comparing the surface morphology of raw and chemically modified lignin-based adsorbents before and after Congo Red (CR) uptake. In Fig. 11(A), the raw CFAL exhibits an irregular, compact, and heterogeneous surface formed by densely packed lignin particles. The texture is rough but largely non-porous, with few clearly developed pores, which is consistent with the only moderate adsorption performance of unmodified CFAL. After exposure to CR, the CFAL surface becomes smoother and appears partly covered by a continuous film in the highlighted regions. This film and the apparent blocking of surface features indicate that CR molecules have deposited on and within the surface, demonstrating effective dye adsorption and strong attachment to the lignin matrix.

In Fig. 11(C), amination leads to a pronounced change in surface structure. The SEM image reveals a more open, porous, and sponge-like morphology with many interconnected pores,[29] in contrast to the denser appearance of CFAL. This increased porosity enlarges the accessible surface area and exposes additional adsorption sites, especially amine groups that can interact electrostatically with the anionic CR dye. The incorporation of hydrophilic, water-attracting amino functionalities into lignin is therefore associated with enhanced dye uptake capacity.[72] In Fig. 11(D–F), which show CR-loaded aminated lignin (AmL–CR) at various magnifications, the initially well-developed porous framework is partly filled or coated by dye. The circled and arrow-indicated regions mark zones where CR has accumulated inside pores; the pore walls there look smoother and darker, consistent with saturation or partial blockage of active sites. Nonetheless, the overall network structure of AmL remains visible, suggesting that the material preserves its mechanical stability after adsorption. Taken together, the images before and after treatment confirm that amination improves both porosity and surface functionality, thereby increasing CR adsorption, while the post-adsorption morphologies clearly evidence successful dye loading and occupation of pores on both CFAL and AmL.

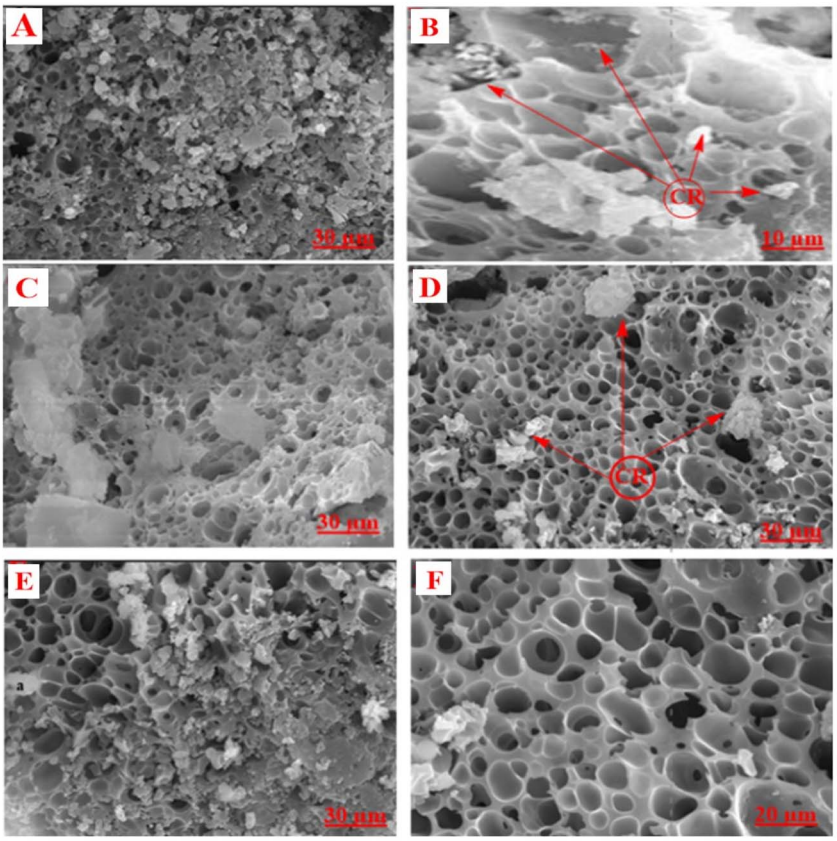

Fig. 11 SEM images of (A) CFAL, (B) CR dye adsorbed CFAL, (C) AmL, and (D–F) CR dye adsorbed AmL.

3.2. Dye removal study of CFAL and AmL samples

3.2.1. Effect of initial concentration and contact time. The adsorption of CR was investigated using Aml and CFAL adsorbents, with a focus on initial concentration and contact time. As shown in Fig. 12(a), the adsorption capacity (Q_t) for AmL increased with both initial concentration and contact time, as a higher concentration provides more dye molecules available for adsorption, reaching an equilibrium adsorption capacity of 38.2 mg g^{-1} at 20 ppm after 80 minutes. In comparison, CFAL (Fig. 12(c)) exhibited a slightly lower adsorption capacity of 35 mg g^{-1} at the same condition. In terms of removal efficiency, AmL demonstrated superior performance, achieving a removal of 95.5%, whereas CFAL removed 87.5% of Congo red at 80 minutes, as illustrated in Fig. 12b and d. However, the removal efficiency tends to decrease at higher concentrations due to the saturation of available active sites on the adsorbent's surface.[72] These results suggest that AmL is more effective in removing Congo red from aqueous solutions, with a higher adsorption capacity and better removal efficiency, making it a more promising material for large-scale wastewater treatment applications.

3.2.2. Effect of pH. The effect of pH on CR adsorption by AmL and CFAL was evaluated as shown in Fig. 13. The adsorption of CR by AmL and CFAL shows optimal removal efficiency at pH 5, with AmL achieving 95.5% and CFAL 87.5% removal efficiency. At this pH, the surface functional groups of both adsorbents are in an ideal deprotonated state, which facilitates strong electrostatic interactions with the negatively charged CR ions ($-SO_3^-$). These favorable interactions enhance the adsorption process. However, at a lower pH of 3, the protonation of functional groups reduces the electrostatic attraction between the adsorbents and dye molecules, resulting in lower removal efficiencies (62.5% for AmL and 53% for CFAL). At higher pH levels of 8 and 10, the alkaline solution renders the adsorbent surface negatively charged, resulting in strong repulsion between the adsorbent and dye molecules, which inhibits the adsorption process.[73]

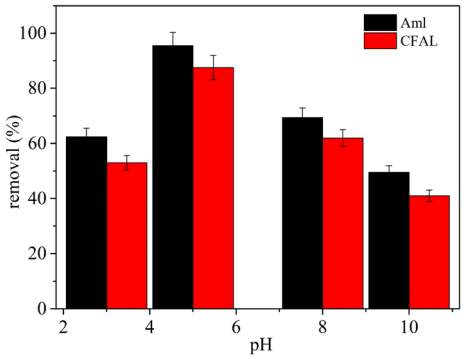

Fig. 13 Effect of pH on CR adsorption by AmL and CFAL.

3.2.3. Effect of adsorbent dosages. Fig. 14 illustrates the effect of adsorbent dose on CR removal by AmL and CFAL, demonstrating a typical adsorption behavior. At lower doses (0.015 g), both materials exhibit higher adsorption capacities (Q_e) due to a greater surface area-to-adsorbent ratio, allowing

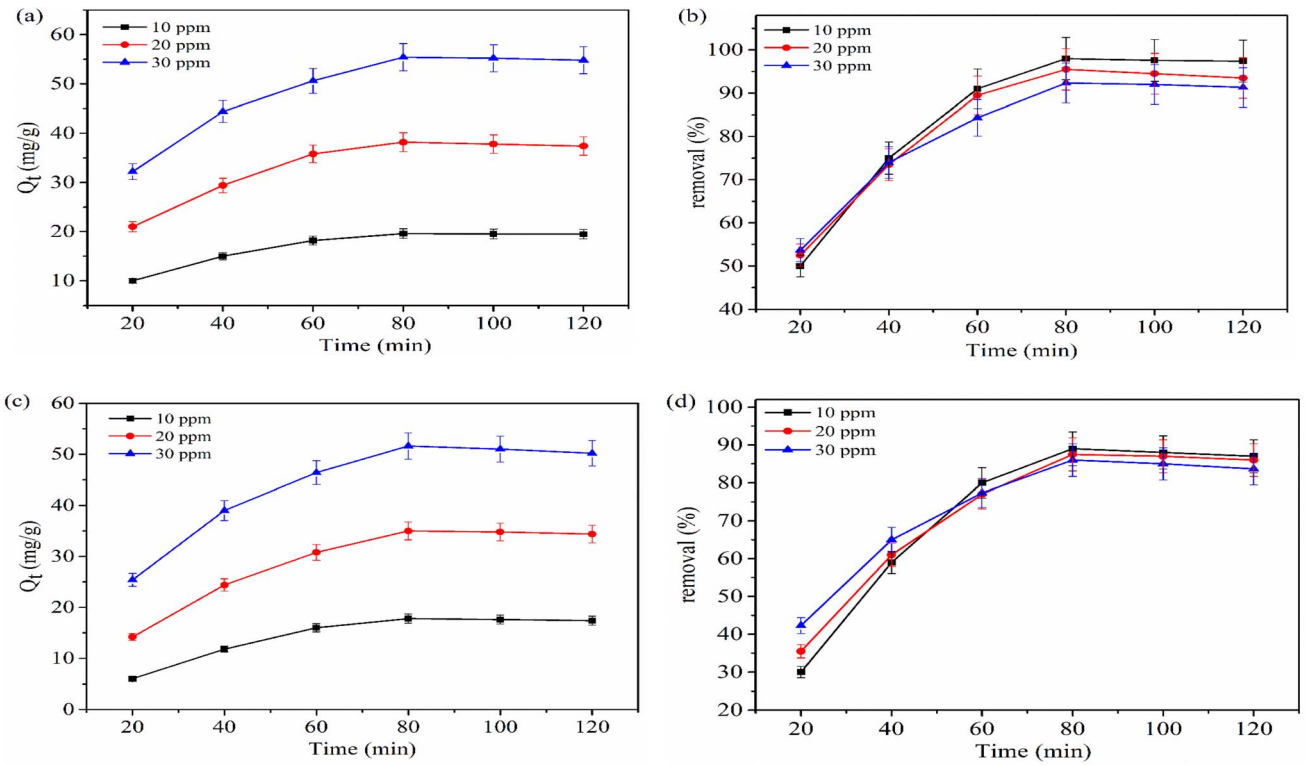

Fig. 12 Effect of initial concentration and contact time on CR adsorption by (a) and (b) Aml, (c) and (d) CFAL.

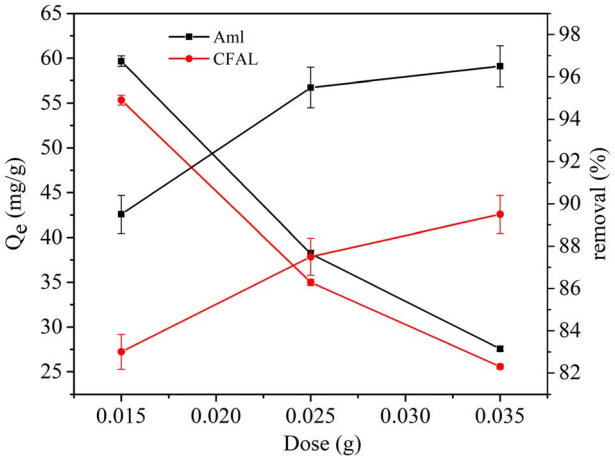

Fig. 14 Effect of adsorbent dose on CR adsorption by AmL and CFAL.

more dye to be adsorbed per gram of material. As the dose increases, the available adsorption sites become saturated, resulting in a decrease in Q_e, although the removal efficiency continues to rise. This is because a higher adsorbent dose provides more available active sites, resulting in improved dye removal. AmL shows higher removal efficiency, reaching 96.5% at 0.035 g, while CFAL achieves 89.5% at the same dose. This behavior suggests that increasing the adsorbent dose enhances CR removal but with diminishing returns in adsorption capacity, indicating the importance of optimizing the adsorbent dose to balance both efficiency and adsorption potential for large-scale applications.[74]

3.2.4. Adsorption kinetics study. Fig. 15 shows the kinetic study of CR adsorption by AmL and CFAL, which was performed using the pseudo-first-order and pseudo-second-order models, which describe the adsorption rate and capacity. Table 7 presents the kinetic parameters of these fitting equations. The pseudo-first-order kinetic model is expressed as

$$Q_t = Q_e[1 - \exp(-K_1 t)] \quad (6)$$

where Q_e is the equilibrium adsorption capacity (mg g^{-1}), Q_t is the adsorption capacity at time t (mg g^{-1}), and K_1 is the pseudo-first-order rate constant (min^{-1}). The pseudo-second-order kinetic model is given by

$$Q_t = \frac{Q_e^2 K_2 t}{[K_2 Q_e t + 1]} \quad (7)$$

where K_2 is the pseudo-second-order rate constant (g mg^{-1} min^{-1}). The kinetic evaluation of CR adsorption onto AmL and CFAL using non-linear models revealed that the PSO model provided the best fit to the experimental data, with higher correlation coefficients (AmL: $R^2 = 0.97$; CFAL: $R^2 = 0.96$) compared with the PFO model (AmL: 0.95; CFAL: 0.94). The PSO-predicted capacities (46.76 mg g^{-1} for AmL and 49.26 mg g^{-1} for CFAL) also agreed more closely with the experimental values, confirming that adsorption is governed by strong affinity-controlled interactions rather than simple physisorption. This behavior is consistent with previous reports where PSO kinetics dominate dye uptake due to surface complexation and electrostatic forces. The higher PFO rate constant of AmL (K_1 = 0.038 min^{-1}) compared with CFAL (0.026 min^{-1}) further indicates faster initial binding, attributable to amine-enhanced active sites. Overall, the kinetic performance demonstrates that CR adsorption on both

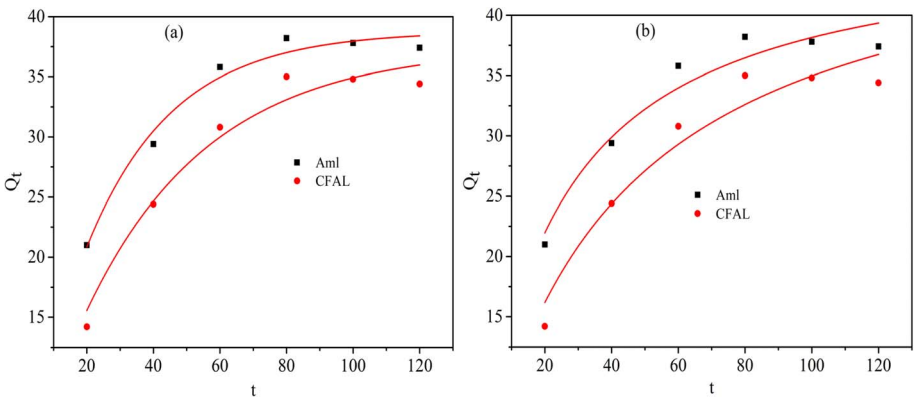

Fig. 15 Non-linear fitting curves on CR adsorption kinetics (a) pseudo-first-order and (b) pseudo-second-order by AmL and CFAL.

Table 7 Kinetic parameters obtained for pseudo-first-order and pseudo-second-order

	Pseudo-first-order			Pseudo-second-order		
Adsorbent	Q_e (mg g^{-1})	K_1 (min^{-1})	R^2	Q_e (mg g^{-1})	K_2 (g mg^{-1} min^{-1})	R^2
Aml	38.77	0.038	0.95	46.76	0.0009	0.97
CFAL	37.46	0.026	0.94	49.26	0.0004	0.96

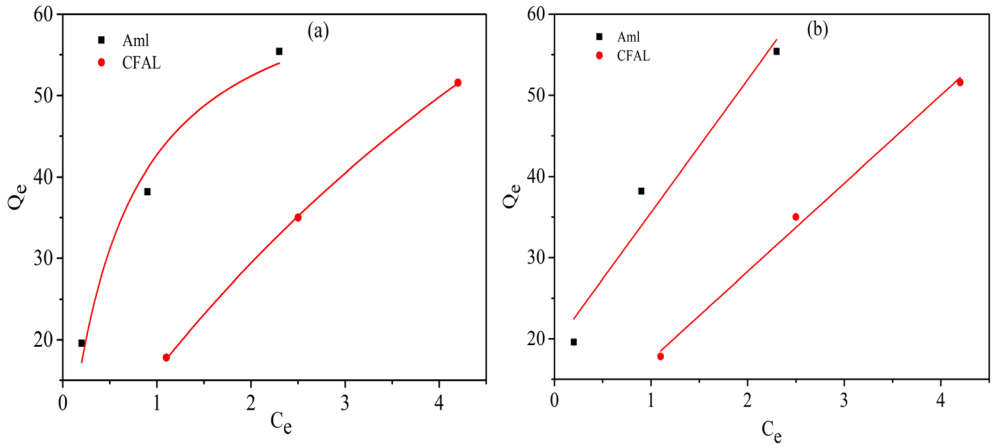

Fig. 16 Adsorption isotherm study on CR adsorption by AmL and CFAL (a) Langmuir and (b) the Freundlich isotherm model.

materials follows a PSO-controlled mechanism, with Aml exhibiting superior adsorption dynamics.[75]

3.2.5. Adsorption isotherm study. Adsorption isotherm studies investigate the adsorption properties of materials and provide essential data to determine whether AmL and CFAL can be utilized as adsorbents. The corresponding isotherm results are presented in Fig. 16. The isotherm uptake parameters were analyzed using the non-linear Langmuir and the Freundlich isotherms, which are given by eqn (8) and (9), respectively.

$$Q_e = \frac{Q_m K_L C_e}{1 + K_L C_e} \quad (8)$$

$$Q_e = K_F C_e^{1/n} \quad (9)$$

where C_e is the adsorbate concentration at equilibrium (mg L^{-1}), Q_m is the maximum adsorption capacity (mg g^{-1}), K_L is the Langmuir constant, K_F and n are the Freundlich constants. The equilibrium data for CR adsorption onto Aml and CFAL are presented in Table 8. The Langmuir model produced an excellent fit for AmL ($R^2 = 0.99$), with a high monolayer capacity ($Q_m = 162.59$ mg g^{-1}), indicating the formation of a uniform monolayer on well-defined active sites. In contrast, CFAL exhibited a lower Q_m (67.79 mg g^{-1}) and slightly weaker correlation ($R^2 = 0.95$), consistent with its less functionalized surface. The Freundlich model also showed strong fitting for Aml ($R^2 = 0.99$) and moderate fitting for CFAL ($R^2 = 0.91$), demonstrating the presence of surface heterogeneity. The Freundlich constants further highlight the higher adsorption affinity of Aml ($K_F = 6.55$ mg g^{-1}) compared with CFAL ($K_F = 19.18$ mg g^{-1}), while the low values of $n < 1$ for both materials suggest a favorable yet intensity-controlled adsorption process, characteristic of lignocellulosic adsorbents. Overall, the combined isotherm analysis confirms that Aml possesses significantly stronger adsorption capacity and more efficient site utilization than CFAL, in agreement with trends reported for amine-functionalized biopolymer adsorbents.[76]

Table 8 Isotherm parameters obtained for CR adsorption by AmL and CFAL

	Langmuir isotherm model			Freundlich isotherm model		
Adsorbent	Q_m (mg g^{-1})	K_L (L mg^{-1})	R^2	n	k_F (mg g^{-1})	R^2
Aml	162.59	0.11	0.99	0.09	6.55	0.99
CFAL	67.79	1.70	0.95	0.06	19.18	0.91

3.2.6. Effect of temperature. The adsorption performance of Aml and CFAL toward CR dye was evaluated at 303–323 K, and the results are presented in Fig. 17. For both adsorbents, the removal efficiency decreased progressively with increasing temperature, confirming that the adsorption of CR is exothermic in nature. At 303 K, Aml achieved the highest removal efficiency (95.5%), while CFAL reached 87.5%. When the temperature increased to 323 K, the removal efficiencies decreased to 85.5% for Aml and 76% for CFAL.

A decline in adsorption capacity with increasing temperature has been frequently reported for anionic dyes on lignin-based and carbonaceous materials. This behavior occurs because

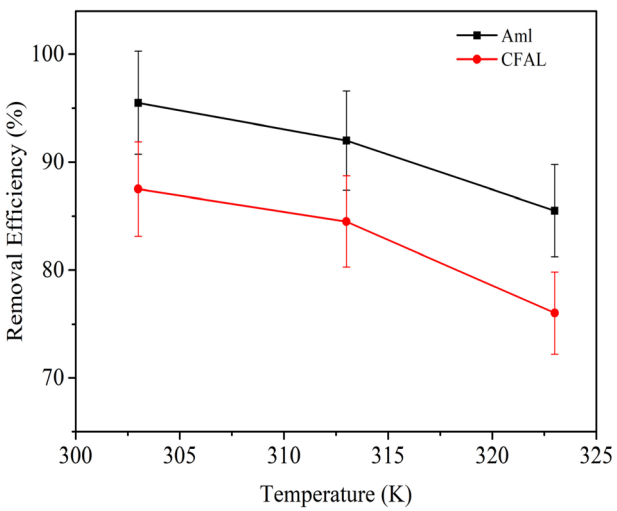

Fig. 17 Effect of temperature on CR adsorption by Aml and CFAL.

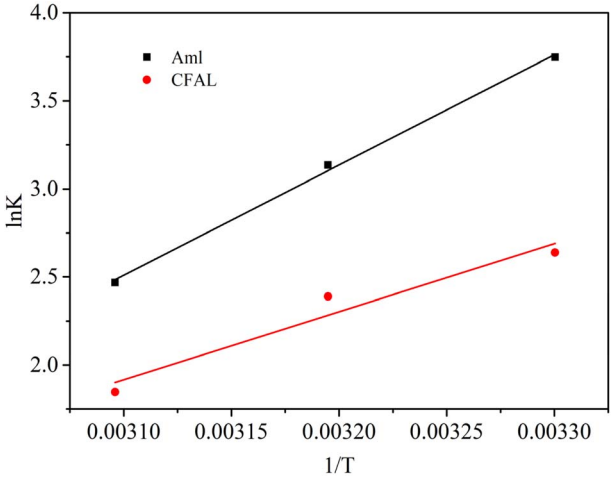

Fig. 18 Thermodynamic study on CR adsorption by Aml and CFAL.

elevated temperatures increase the kinetic energy of dye molecules, reducing the strength of physical interactions such as electrostatic attraction, hydrogen bonding, and π–π interactions between CR and the adsorbent surface. Higher temperature may also enhance the solubility of CR in water, consequently reducing its tendency to migrate toward adsorption sites.[77]

3.2.7. Thermodynamic study. Fig. 18 shows the thermodynamic parameters for CR adsorption on Aml and CFAL were evaluated using the standard Gibbs, Van't Hoff, and equilibrium relations:

$$\Delta G^{\circ} = \Delta H^{\circ} - T\Delta S^{\circ}$$

$$\Delta G^{\circ} = -RT\ln K_c$$

$$\ln K_c = -\frac{\Delta H^{\circ}}{R}\frac{1}{T} + \frac{\Delta S^{\circ}}{R}$$

As shown in Table 9, all ΔG° values are negative, confirming that CR adsorption onto both adsorbents is spontaneous, with decreasing magnitude at higher temperature indicating reduced spontaneity. The adsorption is exothermic, evidenced by the negative ΔH° values (Aml: −52.06 kJ mol^{-1}; CFAL: −32.13 kJ mol^{-1}). These values fall within the range widely reported for physical adsorption of anionic dyes on lignocellulosic and carbonaceous materials, which typically proceed *via* electrostatic interactions, hydrogen bonding, and π–π stacking.[77]

Table 9 Thermodynamic parameters obtained for CR dye adsorption by Aml and CFAL

			−ΔG^0 (kJ mol^{-1})		
	ΔS^0 (kJ mol^{-1})	ΔH^0 (kJ mol^{-1})	303	313	323
Aml	−0.1405	−52.06	9.48	8.07	6.67
CFAL	−0.0836	−32.13	6.77	5.94	5.10

The negative ΔS° values for both Aml and CFAL imply decreased randomness at the solid–liquid interface due to the ordered arrangement of CR molecules upon adsorption. Aml exhibits more negative ΔG° and a higher $|\Delta H^{\circ}|$ than CFAL, indicating a stronger affinity for CR, consistent with reports showing amination enhances interaction strength with sulfonated dyes.

3.2.8. Reusability. The regeneration performance of Aml and CFAL was assessed over four consecutive adsorption–desorption cycles using 0.1 N NaOH as the desorbing agent, which is widely employed for lignin-based adsorbents due to its ability to disrupt electrostatic and hydrogen-bonding interactions between anionic dyes and phenolic/amine sites without degrading the lignin structure. As shown in Fig. 19, Aml exhibited excellent reusability, with removal efficiency decreasing only from 95.5% in the first cycle to 83.4% in the fourth cycle, indicating strong structural stability and effective dye desorption. In contrast, CFAL showed a more pronounced decline, dropping from 87.5% to 72.1% over the same cycles. The superior regeneration of Aml can be attributed to its amine-functional groups, which provide more robust binding sites that remain intact during alkaline desorption. Overall, these results demonstrate that Aml possesses significantly higher operational durability than CFAL, confirming its suitability for repeated wastewater treatment applications.[78]

3.3. Mechanism of adsorption

Micro-bridging and charge neutralization are the two primary mechanisms influencing the dye removal process.[79] The dye removal percentage depends on the size of the cation because an increase in nitrogen content leads to a rise in cationic charge. Charge neutralization was suggested as a potential regulating mechanism to explain this phenomenon. By the synthesis, we got a 6.83% nitrogen content, which is still a very low content. As a result, the dye precipitation technique took longer due to the slow interaction between the cationic AmL and the anionic CR dye. Another key point is that, compared to CFAL, AmL would have a greater surface area. Chen *et al.*[79]

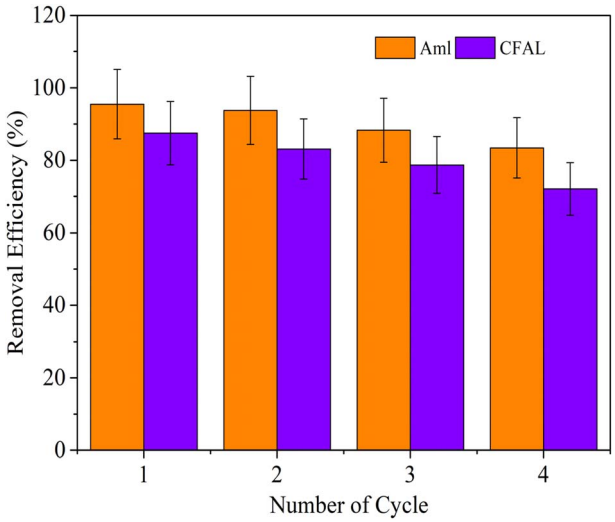

Fig. 19 Reusability of Aml and CFAL on CR adsorption.

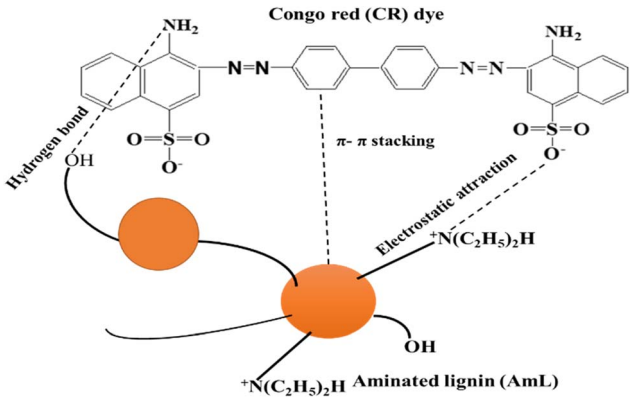

Fig. 20 Proposed mechanisms of CR dye adsorption by AmL in acidic conditions.

investigated the surface area of Klason lignin and AmL, observing BET surface areas of 4.7 and 47.1 $m^2 g^{-1}$, respectively. This indicates that as the surface area of the adsorbent increased, the adsorption capacity also increased. Another critical issue is that the grafted amino group in AmL is protonated under acidic conditions.[69] As a result, a positive charge was introduced on the surface of AmL, leading to increased interaction between the positively charged AmL and the negatively charged CR dye, which in turn resulted in a higher removal percentage of the CR dye. It is widely accepted that the mechanism of lignin-derived adsorbents is *via* hydrogen bonding, π–π stacking, and electrostatic interactions.[80,81] The proposed adsorption mechanisms of the anionic dye (CR) are shown in Fig. 20. Under acidic conditions, the anionic CR dye can be attracted by AmL through electrostatic attraction. When the pH increased, the adsorption capacity for CR decreased due to the electrostatic repulsion force under alkaline conditions, which prevented the adsorption of CR. Therefore, acidic conditions are more suitable for the adsorption of anionic dyes (CR).

3.4. Computational analysis

3.4.1. Mechanism: insights from DFT and TD-DFT studies. To achieve a molecular-level understanding of the structural and electronic changes caused by amination, DFT and TD-DFT calculations were conducted at the B3LYP/6-31(d) level, as shown in the Fig. 21. The computed HOMO–LUMO energy gap for lignin was 4.761 eV, while for AmL, this gap slightly reduced to 4.747 eV. This reduction in the band gap for AmL indicates enhanced electronic conjugation and better charge delocalization, which can be linked to the addition of electron-rich nitrogen groups [$-N(C_2H_5)_2^-$].[82–84] Such electronic adjustments are beneficial for electron transfer processes and are anticipated to enhance dye–adsorbent interactions. Time-dependent DFT (TD-DFT) calculations offered further insights into the properties of the excited states. For CFAL, the first singlet excited-state transition (S_1) occurred at 4.5682 eV (271.41 nm) with a moderate oscillator strength (f = 0.2002), primarily driven by π → π* transitions within the aromatic structure. In AmL, the corresponding S_1 transition was observed at 4.5392 eV (273.14 nm),

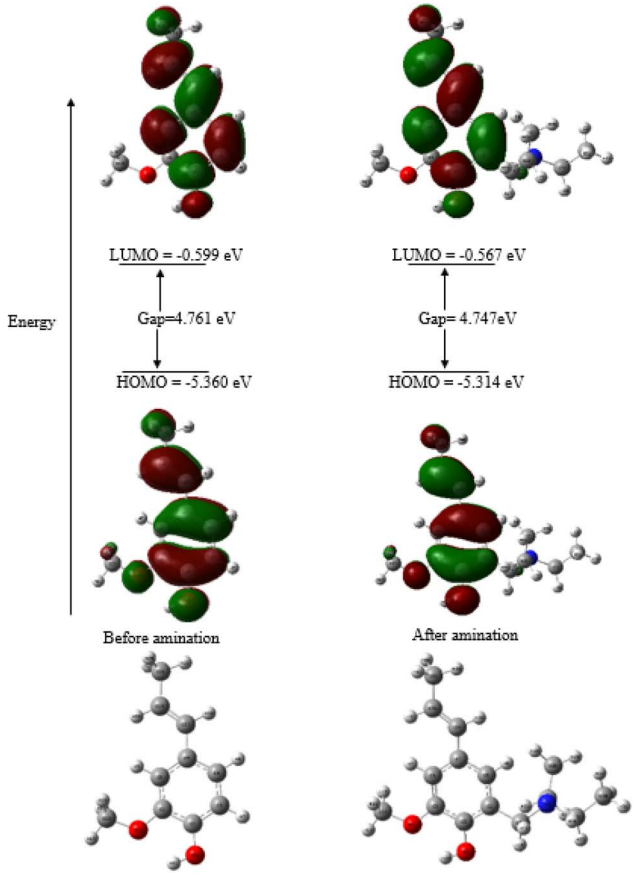

Fig. 21 HOMO–LUMO orbital distributions of CFAL and AmL. The figure illustrates the spatial distribution of the highest occupied molecular orbitals (HOMO) and lowest unoccupied molecular orbitals (LUMO), highlighting the electron density localization before and after amination. The results show that nitrogen functionalization in AmL increases electron delocalization and reduces the HOMO–LUMO energy gap, which can facilitate electron transitions. Gray, red, blue, and light gray spheres represent carbon, oxygen, nitrogen, and hydrogen atoms, respectively.

with a very low oscillator strength (f = 0.0010), indicating partial n → π* character due to contributions from nitrogen lone pairs.[84,85] Amination enhances π–π conjugation and introduces n → π* transitions, promoting redshifted emission in amino-functionalized systems.[86–88] Hydrogen bonding increases molecular rigidity, reducing non-radiative decay pathways. Both intra- and intermolecular hydrogen bonds stabilize through–space interactions ($n\cdots$n and $n\cdots\pi$), restricting torsional motion and improving radiative recombination.[89–91] This slight redshift in absorption wavelength suggests stabilization of the LUMO level and a lower excitation energy barrier in AmL compared to CFAL. Higher-lying excited states in AmL (S_2 at 4.5514 eV, 272.41 nm, f = 0.1436; S_3 at 4.9030 eV, 252.88 nm, f = 0.3125) showed stronger absorption intensities, reflecting a combination of n → π* and π → π* transitions introduced by amination. The functional groups reduce the energy bandgap in EL, facilitating electron transitions and promoting the n → π transition. This confirms that the emission of AmL predominantly originates from the n → π transitions of the amine groups.[88] Overall, the DFT and TD-DFT

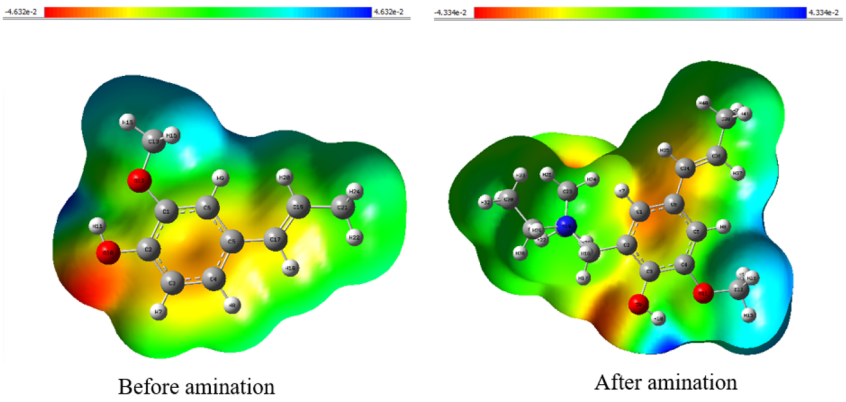

Fig. 22 Electrostatic potential maps of CFAL and AmL. Red and blue indicate electron-rich and electron-deficient regions, respectively.

results consistently demonstrate that amination of CFAL decreases the band gap, stabilizes excited states, and enhances charge delocalization. These theoretical findings support the experimental results by confirming that electronic modification through amination promotes improved optical activity and facilitates charge-transfer processes, which in turn contribute to the superior dye adsorption capacity of AmL compared to CFAL.

3.4.2. Electrostatic potential (ESP) mapping. ESP maps Fig. 22 further illustrate the effect of amination. ESP mapping reveals more uniform charge distribution in AmL, with increased polarity and localized electron-rich regions that act as active sites for dye binding.[92] For native lignin, the ESP surface spanned from -4.632×10^{-2} a.u. (electron-rich domains) to $+4.632 \times 10^{-2}$ a.u. (electron-deficient domains), reflecting a strongly polarized surface. In contrast, aminated lignin exhibited slightly moderated values (-4.334×10^{-2} to $+4.334 \times 10^{-2}$ a.u.), indicating a reduction in the extremes of charge localization. This softening of surface polarity arises from the delocalization induced by nitrogen functionalities, which reduces localized electrostatic "hotspots" and promotes more uniform charge distribution. Such moderation enhances the availability of multiple adsorption sites, thereby facilitating stronger electrostatic interactions and hydrogen bonding with anionic dyes like CR.

4. Conclusion

Lignin was successfully isolated from green coconut husk waste (CFAL) and aminated *via* the Mannich reaction to obtain AmL with a nitrogen content of 6.83%. Structural analyses (FTIR, ^{1}H NMR, and XRD) confirmed the introduction of amino groups, and AmL does not introduce a new crystalline phase. Although AmL exhibited slightly lower thermal stability than CFAL, its adsorption performance was markedly superior. AmL demonstrated superior removal efficiency, achieving 95.5% CR dye adsorption under optimal acidic conditions, primarily due to the presence of $-N(C_2H_5)_2$ groups that facilitate stronger electrostatic interactions and hydrogen bonding with anionic dye molecules. Thermodynamic analysis indicated that CR adsorption onto both CFAL and AmL is spontaneous, exothermic, and entropy-decreasing, with AmL exhibiting a more negative ΔH° (-52.06 kJ mol^{-1}) and ΔG°, signifying stronger dye–adsorbent affinity compared to CFAL. Reusability tests further revealed the practical advantages of AmL, which maintained 83.4% removal efficiency after four adsorption–desorption cycles, outperforming CFAL and demonstrating excellent structural stability under repeated use. Derived from renewable biomass, AmL represents a cost-effective and environmentally sustainable alternative for wastewater treatment with strong potential for industrial application. Complementary DFT and TD-DFT studies revealed that amination reduces the HOMO–LUMO gap, increases electron delocalization, and promotes a more uniform surface charge distribution. ESP mapping further indicated the presence of enhanced active sites for hydrogen bonding and electrostatic interactions with anionic dyes. These theoretical insights align with experimental findings, confirming that nitrogen functionalization improves charge-transfer efficiency and adsorption affinity, thereby validating the superior performance of AmL as a bio-adsorbent.

Author contributions

Riyadh Hossen Bhuiyan: investigation, methodology, formal analysis, data analysis, writing – original draft and editing; Mohammad Mahbubur Rahman: idea generation, conceptualization, supervision, validation, funding acquisition, writing – review and editing; Md. Masum Billah: methodology, investigation, formal analysis, writing – reviewing and editing; Taslima Akter: methodology, investigation, formal analysis, writing – reviewing and editing; Md. Fardin Ehsan: methodology, investigation, writing – reviewing and editing; Md. Shakhawoat Hossain: methodology, investigation, formal analysis, writing – reviewing and editing; Mamunur Rashid: methodology, investigation, formal analysis, writing – reviewing and editing; Md. Saiful Islam: methodology, investigation, formal analysis, writing – reviewing and editing; Swapan Kumer Ray: conceptualization, supervision, validation, funding acquisition, writing – review and editing.

Conflicts of interest

The authors declare that they have no known competing financial interests or personal relationships that could have appeared to influence the work reported in this paper.

Data availability

All data supporting the findings of this study are included in the main manuscript. Raw data are available from the corresponding author upon reasonable request.

Acknowledgements

The authors acknowledge Bangladesh Council of Scientific and Industrial Research for support to carry out the research work.

References

1 H. Zhang, K. Xue, B. Wang, W. Ren, D. Sun, C. Shao and R. Sun, *Bioresour. Technol.*, 2024, **395**, 130347.
2 F. Ahmadijokani, A. Ghaffarkhah, H. Molavi, S. Dutta, Y. Lu, S. Wuttke and M. Arjmand, *Adv. Funct. Mater.*, 2024, **34**, 2305527.
3 A. Ejsmont, S. Dutta, A. Jankowska, S. Wuttke and J. Goscianska, *Chem. Mater.*, 2024, **36**, 4468–4480.
4 S. Dutta, A. Sinelshchikova, J. Andreo and S. Wuttke, *Nanoscale Horiz.*, 2024, **9**, 885–899.
5 S. Moyo, B. P. Makhanya and P. E. Zwane, *Heliyon*, 2022, **8**, e09632.
6 B. A. Kusumlata, A. Kumar and S. Gautam, *Limnol. Rev.*, 2024, **24**, 126–149.
7 A. Kanwal, R. Rehman, M. Imran, G. Samin, M. M. Jahangir and S. Ali, *RSC Adv.*, 2023, **13**, 26455–26474.
8 A. Nyabadza, M. Makhesana, A. Plouze, A. Kumar, I. Ramirez, S. Krishnamurthy, M. Vazquez and D. Brabazon, *J. Environ. Chem. Eng.*, 2024, **12**, 112643.
9 N. Zakaria, R. Rohani, W. H. M. Wan Mohtar, R. Purwadi, G. A. Sumampouw and A. Indarto, *Water*, 2023, **15**, 1339.
10 G. G. Msemwa, M. Nasr, A. Abdelhaleem, M. Fujii and M. G. Ibrahim, *Water, Air, Soil Pollut.*, 2025, **236**, 57.
11 S. Dutta, B. Gupta, S. K. Srivastava and A. K. Gupta, *Mater. Adv.*, 2021, **2**, 4497–4531.
12 R. Vinodh, R. Padmavathi and D. Sangeetha, *Desalination*, 2011, **267**, 267–276.
13 Z. Zeitoun and N. Y. Selem, *Bull. Natl. Res. Cent.*, 2023, **47**, 153.
14 N. Y. Donkadokula, A. K. Kola, I. Naz and D. Saroj, *Rev. Environ. Sci. Biotechnol.*, 2020, **19**, 543–560.
15 W. Al-Gethami, M. A. Qamar, M. Shariq, A.-N. M. A. Alaghaz, A. Farhan, A. A. Areshi and M. H. Alnasir, *RSC Adv.*, 2024, **14**, 2804–2834.
16 Y. Liu, B. Biswas, M. Hassan and R. Naidu, *Processes*, 2024, **12**, 1195.
17 C. Poornachandhra, R. M. Jayabalakrishnan, M. Prasanthrajan, G. Balasubramanian, A. Lakshmanan, S. Selvakumar and J. E. John, *RSC Adv.*, 2023, **13**, 4757–4774.
18 A. Haleem, A. Shafiq, S.-Q. Chen and M. Nazar, *Molecules*, 2023, **28**, 1081.
19 A. P. Periyasamy, *Sustainability*, 2024, **16**, 495.
20 A. Strebel, M. Behringer, H. Hilbig, A. Machner and B. Helmreich, *Front. Environ. Eng.*, 2024, **3**, 1347981.
21 T. D. Pham, V. P. Bui, T. N. Pham, T. M. D. Le, K. T. Nguyen, V. H. Bui and T. D. Nguyen, *Polymers*, 2021, **13**, 1536.
22 M. Yadav, N. Singh, Annu, S. A. Khan, C. J. Raorane and D. K. Shin, *Polymers*, 2024, **16**, 2417.
23 M. Kajihara, D. Aoki, Y. Matsushita and K. Fukushima, *J. Appl. Polym. Sci.*, 2018, **135**, 46611.
24 X. Meng, Y. Li, J. Liu, Q. Wang, X. Zhang and H. Sun, *ACS Omega*, 2020, **5**, 2865–2877.
25 N.-E. El Mansouri and J. Salvadó, *Ind. Crops Prod.*, 2007, **26**, 116–124.
26 S. Gao, Y. Zhao, X. Zhang, J. Wang, Y. Zhang and G. Chen, *Chem. Eng. J.*, 2020, **394**, 124896.
27 S. Debnath, N. Ballav, A. Maity and K. Pillay, *Int. J. Biol. Macromol.*, 2015, **75**, 199–209.
28 X. Guo, S. Zhang and X. Shan, *J. Hazard. Mater.*, 2008, **151**, 134–142.
29 Y. Wu, S. Zhang, X. Guo and H. Huang, *Bioresour. Technol.*, 2008, **99**, 7709–7715.
30 N. Ballav, S. Debnath, K. Pillay and A. Maity, *J. Mol. Liq.*, 2015, **209**, 387–396.
31 J. Domínguez-Robles, M. S. Peresin, T. Tamminen, A. Rodríguez, E. Larrañeta and A.-S. Jääskeläinen, *Int. J. Biol. Macromol.*, 2018, **115**, 1249–1259.
32 C. Yu, F. Wang, C. Zhang, S. Fu and L. A. Lucia, *React. Funct. Polym.*, 2016, **106**, 137–142.
33 A. B. Albadarin, M. N. Collins, M. Naushad, S. Shirazian, G. Walker and C. Mangwandi, *Chem. Eng. J.*, 2017, **307**, 264–272.
34 M. Wawrzkiewicz, P. Bartczak and T. Jesionowski, *Int. J. Biol. Macromol.*, 2017, **99**, 754–764.
35 D. Parajuli, H. Kawakita, K. Inoue and M. Funaoka, *Ind. Eng. Chem. Res.*, 2006, **45**, 6405–6412.
36 X. Wang, Y. Zhang, C. Hao, X. Dai, Z. Zhou and N. Si, *RSC Adv.*, 2014, **4**, 28156–28164.
37 J. W. Heo, L. An, J. Chen, J. H. Bae and Y. S. Kim, *Chemosphere*, 2022, **295**, 133815.
38 M. Sarwar Jahan, M. Shamsuzzaman, M. M. Rahman, S. M. Iqbal Moeiz and Y. Ni, *Ind. Crops Prod.*, 2012, **37**, 164–169.
39 N. H. A. Latif, N. Brosse, I. Ziegler-Devin, L. Chrusiel, R. Hashim and M. H. Hussin, *BioResources*, 2021, **17**, 469–491.
40 M. A. Gilarranz, F. Rodriguez, M. Oliet and J. A. Revenga, *Sep. Sci. Technol.*, 1998, **33**, 1359–1377.
41 Y. Matsushita and S. Yasuda, *J. Wood Sci.*, 2003, **49**, 166–171.
42 G.-J. Jiao, P. Peng, S.-L. Sun, Z.-C. Geng and D. She, *Int. J. Biol. Macromol.*, 2019, **127**, 544–554.
43 S. McArdle, S. Endo, A. Aspuru-Guzik, S. C. Benjamin and X. Yuan, *Rev. Mod. Phys.*, 2020, **92**, 015003.
44 J. Tirado-Rives and W. L. Jorgensen, *J. Chem. Theory Comput.*, 2008, **4**, 297–306.
45 Y. Takano and K. N. Houk, *J. Chem. Theory Comput.*, 2005, **1**, 70–77.
46 I. B. Obot, D. D. Macdonald and Z. M. Gasem, *Corros. Sci.*, 2015, **99**, 1–30.
47 A. Sluiter, B. Hames, R. Ruiz, C. Scarlata, J. Sluiter, D. Templeton and D. Crocker, *Technical Report*, National Renewable Energy Laboratory, 2008.

48 *The Chemistry of Solid Wood, Advances in Chemistry*, ed. R. Rowell, American Chemical Society, Washington, DC, 1984, vol. 207.
49 L. A. Panamgama and P. R. U. S. K. Peramune, *Int. J. Biol. Macromol.*, 2018, **113**, 1149–1157.
50 M. A. Gilarranz, F. Rodriguez, M. Oliet and J. A. Revenga, *Sep. Sci. Technol.*, 1998, **33**, 1359–1377.
51 A. Lourenço, J. Gominho, A. V. Marques and H. Pereira, *Bioresour. Technol.*, 2012, **123**, 296–302.
52 H. Hatakeyama and T. Hatakeyama, in *Biopolymers: Lignin, Proteins, Bioactive Nanocomposites*, ed. A. Abe, K. Dusek and S. Kobayashi, Springer, Berlin, Heidelberg, 2010, pp. 1–63.
53 J. Qiu, Y. Zhang, L. Wang, H. Li, Z. Wu and X. Zhang, *Int. J. Biol. Macromol.*, 2023, **233**, 123547.
54 X. Du, J. Li and M. E. Lindström, *Ind. Crops Prod.*, 2014, **52**, 729–735.
55 H. Pan, G. Sun and T. Zhao, *Int. J. Biol. Macromol.*, 2013, **59**, 221–226.
56 B. Seemala, S. B. Chikkula, P. C. Acharjee, M. D. Jones, L. G. Peeva and T. Welton, *ACS Sustain. Chem. Eng.*, 2018, **6**, 10587–10594.
57 P. J. Flory, *Principles of Polymer Chemistry*, Cornell University Press, Ithaca, NY, 1953.
58 D. Meier, V. Zúñiga-Partida, F. Ramírez-Cano, N.-C. Hahn and O. Faix, *Bioresour. Technol.*, 1994, **49**, 121–128.
59 M. Alekhina, O. Ershova, A. Ebert, S. Heikkinen and H. Sixta, *Ind. Crops Prod.*, 2015, **66**, 220–228.
60 A. Abdulkhani, H. M. Akbarpour, M. T. Ahmadi, M. Yousefi, H. Sixta and R. Behzadfar, *Biomass Convers. Biorefinery*, 2024, **14**, 8639–8647.
61 T. Mălu□an, R. Nicu and V. I. Popa, *BioResources*, 2008, **3**(1), 13–20.
62 G. K. Oloyede, B. O. Ogunsile, M. S. Ali and W. A. Ngouonpe, *J. Chem. Soc. Niger.*, 2019, **44**, 7.
63 M. Kollman, X. Jiang, S. J. Thompson, O. Mante, D. C. Dayton, H. M. Chang and H. Jameel, *Green Chem.*, 2021, **23**, 7122–7136.
64 B. Wang, T. Y. Chen, H. M. Wang, H. Y. Li, C. F. Liu and J. L. Wen, *Int. J. Biol. Macromol.*, 2018, **107**, 426–435.
65 M. P. Slacke, B. Riedl and T. Stevanovic-Janezic, in *Proc. 5th Eur. Workshop on Lignocellulosics and Pulp*, University of Aveiro, 1998, pp. 325–327.
66 B. B. Hallac, P. Sannigrahi, Y. Pu, M. Ray, R. J. Murphy and A. J. Ragauskas, *J. Agric. Food Chem.*, 2009, **57**, 1275–1281.
67 S. Li and K. Lundquist, *Nord. Pulp Pap. Res. J.*, 1994, **9**, 191–195.
68 A. Goudarzi, L.-T. Lin and F. K. Ko, *J. Nanotechnol. Eng. Med.*, 2014, **5**, 021006.
69 R. S. Rohella, N. Sahoo, S. C. Paul, S. Choudhury and V. Chakravortty, *Thermochim. Acta*, 1996, **287**, 131–138.
70 K. Samit, Y. S. Negi and J. S. Upadhyaya, *Adv. Mater. Lett.*, 2010, **1**, 246–253.
71 A. Monshi, M. R. Foroughi, M. R. Monshi and J. World, *Nano Sci. Eng.*, 2012, **2**, 154–160.
72 A. Zourou, S. Tzereme, G. N. Karanikolos and D. Bikiaris, *Carbon Trends*, 2022, **7**, 100147.
73 R. S. de Farias, H. L. de B. Buarque, M. R. da Cruz, L. M. F. Cardoso, T. de A. Gondim and V. R. de Paulo, *Eng. Sanit. Ambient.*, 2018, **23**, 1053–1060.
74 T. Guo and C. Bulin, *Res. Chem. Intermed.*, 2021, **47**, 945–971.
75 E. C. Lima, F. Sher, A. Guleria, M. R. Saeb, I. Anastopoulos, H. N. Tran and A. Hosseini-Bandegharaei, *J. Environ. Chem. Eng.*, 2021, **9**, 104813.
76 L. Fang, H. Wu, Y. Shi, Y. Tao and Q. Yong, *Front. Bioeng. Biotechnol.*, 2021, **9**, 691528.
77 Z. R. Zair, Z. T. Alismaeel, M. Y. Eyssa and M. J. M-Ridha, *Heat Mass Transfer*, 2022, **58**, 1393–1410.
78 M. M. Billah, S. P. Shandhi, M. R. Naim, M. B. Mesbah, S. A. Eti, M. Kamruzzaman and M. A. Hoque, *Surf. Interfaces*, 2025, **74**, 107655, DOI: 10.1016/j.surfin.2025.107655.
79 J. Chen, L. An, J. W. Heo, J. H. Bae, H. Jeong and Y. S. Kim, *J. Wood Chem. Technol.*, 2022, **42**, 114–124.
80 Q. Wu, X. Ye, Y. Lv, R. Pei, M. Wu and M. Liu, *Chemosphere*, 2020, **258**, 127276.
81 Y. Tan, X. Wang, F. Xiong, J. Ding, Y. Qing and Y. Wu, *Ind. Crops Prod.*, 2021, **171**, 113980.
82 H. Lu, L. Feng, S. Li, J. Zhang, H. Lu and S. Feng, *Macromolecules*, 2015, **48**, 476–482.
83 Z. Zhang, W. Yan, D. Dang, H. Zhang, J. Z. Sun and B. Z. Tang, *Cell Rep. Phys. Sci.*, 2022, **3**, 100716.
84 R. Orita, H. Kondo, T. Kamada, K. Tani, Y. Hatanaka, K. Fujii, Y. Inoue and T. Nabeshima, *Phys. Chem. Chem. Phys.*, 2018, **20**, 16033–16044.
85 R. Wang, H. Fan, W. Jiang, G. Ni and S. Qu, *Appl. Surf. Sci.*, 2019, **467–468**, 446–455.
86 G. S. Kumar, R. R. Nair, M. T. Ramesan, K. R. V. Subramanian and A. Jayakumar, *Nanoscale*, 2014, **6**, 3384–3391.
87 N. Kanlayakan and N. Kungwan, *J. Lumin.*, 2021, **238**, 118260.
88 S. H. Jin, D. H. Kim, G. H. Jun, S. H. Hong and S. Jeon, *ACS Nano*, 2013, **7**, 1239–1245.
89 Z. Demircioğlu, Ç. Albayrak Kaştaş and O. Büyükgüngör, *Spectrochim. Acta, Part A*, 2015, **139**, 539–548.
90 C. Shang, L. Zhang, Q. Jiang, Y. Li, W. Feng, J. Wang and Z. Zhang, *J. Mater. Chem. C*, 2017, **5**, 8082–8090.
91 X. Chen, W. Luo, H. Ma, Q. Peng, W. Z. Yuan and Y. Zhang, *Sci. China Chem.*, 2018, **61**, 351–359.
92 L. Cheng, Y. Ji, X. Liu, L. Mu and J. Zhu, *Chem. Eng. Sci.*, 2021, **242**, 116739.